New Atomic Data For Iron-Peak Elements For Use In Astrophysical Modeling

by

Nathalia Alzate

A thesis submitted to the Graduate Faculty of
Auburn University
in partial fulfillment of the
requirements for the Degree of
Master of Science

Auburn, Alabama
December 14, 2013

Keywords: Supernovae, supernova remnants, W49B, metallicity, abundances, Fe-peak He-like elements, two-photon transition, photon emissivity coefficients, spectra, new atomic data

Approved by

Stuart D. Loch, Chair, Professor of Physics
Connor P. Ballance, Co-Chair, Research Professor of Physics
Michael R. Fogle, Assistant Professor of Physics
Edward Thomas, Professor of Physics
Dean Hoffman, Professor of Mathematics and Statistics

Abstract

Supernovae (SN) and supernova remnant (SNR) plasmas represent some of the most extreme and unusual objects in the universe. X-ray spectra of supernova remnant plasmas are key to understanding the mechanism and dynamics of supernova explosions. In recent years, there have been observations of Cr and Mn X-ray emission lines from a wide range of supernova remnant plasmas. Diagnostics that use these emission features are currently hampered by a lack of atomic data for these Fe-peak elements. The purpose of this research is to generate the high quality atomic data needed by the astrophysics community. We focus on the atomic data for He-like Fe-peak elements Cr^{22+}, Mn^{23+}, Fe^{24+}, Co^{25+}, and Ni^{26+}. As an example of the use of this new data, our spectral analysis is carried out for the Galactic supernova remnant W49B.

The new electron-impact excitation data are calculated using a Dirac R-matrix suite of codes and include the infinite energy limit points on the collision strengths. The data are compared with available literature values, including recent Dirac R-matrix calculations, quantifying the influence of radiation damping and relativistic effects on the new collision data. This dataset includes calculated dipole and non-dipole radiative rates. For each ion, level-resolved electron-impact excitation cross sections and Maxwellian rate coefficients are generated for the 1s nl configurations for 1s $< nl <$ 5g. He-like Kα photon emissivities are calculated for each ion, and the importance of including the two photon transition is shown.

The photon emissivity coefficients (PECs) are used, along with previously calculated data for the H-like ion stages, to investigate the evidence of overionization in the SNR plasma W49B. The He-like data are then used to determine relative abundances of Cr and Mn to Fe in W49B. The role of recombination as a populating mechanism for the He-like line emission is investigated. We discuss the implications of this work, both for the general diagnostics using these He-like lines, and in answering some of the current uncertainties over the nature and makeup of W49B.

Acknowledgments

I would like to start by thanking my advisor, Dr. Stuart Loch, for his guidance and patience throughout this project. Dr. Loch, you have been an amazing mentor during these past few years and it has been an honor working with you. This project has been the most challenging work I have done throughout my academic career and I am eternally grateful for this opportunity. Because of the incredible research that you do and the passion with which you communicate your work, you have instilled in me a thirst for knowledge about a field of physics that I never even considered exploring before coming to Auburn University. Furthermore, your guidance throughout my studies have allowed me to find myself as a student and future researcher. I have excelled in my work because of the vision, encouragement, instruction, and advice you have provided. Thank you especially for always seeing my potential and recognizing my hard work and dedication. I will always carry that with me. I hope to have the opportunity of working with you again.

I would also like to thank my co-advisor, Dr. Connor Ballance, for his immense support during this project. Dr. Ballance, thank you for your guidance during my computational training! With your help, I was able to understand the computational aspects of this project and learn many transferable computational skills. Thanks for the patience and humor!

My appreciation is extended to my thesis committee members, Dr. M. Fogle, Dr. E. Thomas, and Dr. D. Hoffman, for their time and support. Thank you for your comments and discussions that have helped improve this work and spark new ideas for future work.

Finally, special thanks go out to my friends and supporters. Thank you for listening to my frustrations and encouraging me to keep going. You have been my support system during my time at Auburn and have guided me through the tears and the laughter. Sara, your words will stay with me always. Erica and Keith, how do you guys put up with me?

Thank you for adding meaning to my life in Auburn outside my office. You guys are the best and I love you!

Mom and dad, thank you for your never-ending support and patience. Dad, the stubborness, impatience, and humor I get from you has pushed me to work hard and consistently in order to accomplish my goals and enjoy my work. Mom, from you I get your intellect, your thirst for knowledge, your magical perspective on life, and your melancholic way of thinking. Without those things, I wouldn't be able to find a purpose in my life. I love you both!

[Mami y papi, gracias por el apoyo y la paciencia que nunca acaba. Papi, mi terquedad, impaciencia, y humor que provienen de ti me han llevado a seguir trabajando duro para cumplir mis metas y disfrutar mi trabajo. Mami, de ti tengo la intellectualidad, la sed por el conocimiento, tu perspectiva mágica hacia la vida, y tu forma melancólica de pensar. Sin esas cosas, no podría encontrarle propósito a mi vida. Los quiero mucho!]

"In the depths of winter I finally learned that within me there lay an invincible summer."

Albert Camus

Table of Contents

Abstract ii

Acknowledgments iv

List of Figures ix

List of Tables xv

1 Introduction and Background Theory 1

1.1 Introduction 1

1.1.1 Supernovae and Supernova Remnants 1

1.1.2 Observations of supernova remnants 6

1.1.3 Previous X-Ray Observations of Cr and Mn 12

1.1.4 Overview of atomic data for He-like Fe-peak elements 15

1.1.5 Fe-Peak Elements for Use in Diagnostics 16

1.2 Spectral Modeling 17

1.2.1 Collisional Radiative Modeling and Photon Emissivity Coefficients . . 17

1.2.2 Diagnostics of Fractional and Elemental Abundances 21

1.3 R-Matrix Theory 23

1.3.1 Semi-Relativistic Intermediate Coupling Frame Transformation (ICFT) Method 27

1.3.2 Dirac Atomic R-Matrix Code (DARC) 29

1.4 Thesis Objectives and Impact 30

2 Atomic Data Results 31

2.1 Atomic Structure 31

2.2 Collision Strengths 36

2.3 Effective Collision Strengths 40

2.4 Photon Emissivity Coefficients (PEC) 42

3 Spectral Modeling and Abundances 51

3.1 Fractional Abundances 51

3.2 Elemental Abundances 53

4 Discussion and Conclusions 55

4.1 Future Studies 55

Bibliography 57

Appendices 61

Appendix A 61

Appendix B 66

Appendix C 70

List of Figures

1.1 Schematic of a core-collapse supernova explosion. Figure a) shows fusion of elements in a massive star. Figure b) shows the core when it reaches the Chandrasekhar-mass and starts to collapse. In figure c) the inner core compresses into neutrons and the gravitational energy is converted into neutrinos. Figure d) shows the outward-propagating shock wave (red). (e) The shock begins to stall as nuclear processes drain energy away, but it is re-invigorated by interaction with neutrinos. (f) The material outside the inner core is ejected, leaving behind only a degenerate remnant. Illustration by R.J. Hall [GFDL (http://www.gnu.org/copyleft/fdl.html), CC-BY-SA-3.0. 2

1.2 Time-dependent ionization balance for Fe. The Fe ions are assumed to start as neutral and the electron temperature and density are kept constant (N_e=10 cm^{-3} and T_e=2 keV). Note that for clarity only, selected ion stages are shown in the plot. The stars show the equilibrium fractional abundances for the He-like and H-like ion stages for a 2 keV plasma. 5

1.3 Images of W49B. The top figure shows the Digitized Sky Survey (DSS) optical image, the bottom left shows the infra-red image, and the bottom right hand image shows the X-ray image. Note that they are all in the same field of view. . 6

1.4 Supernova remnant Cassiopeia (Cas A) at optical wavelength. 8

1.5 CHANDRA X-ray image of supernova remnant Cas A. 8

1.6 X-ray spectrum of W49B, taken from Miceli et al. [2]. The two different spectra are the results from the two spectrometers on the XMM-Newton telescope. The spectral lines are identified in the figure, while the strong background continuum is due to thermal Bremsstrahlung radiation. 9

1.7 The Cr and Mn X-ray spectral features of W49B, taken from [1]. The first spectral line is of He-like Cr while the second is of He-like Mn. 10

1.8 Grotrian diagram for He-like systems, showing the spontaneous emission transitions. 11

1.9 X-ray spectra of Cas A, taken using the CHANDRA X-ray observatory. 13

1.10 Schematic showing the mechanisms for populating and depopulating a level in Fe^{24+}. The processes include spontaneous emission ($A_{i\to j}$), electron-impact excitation and de-excitation (q), electron-impact ionization (S) and electron-recombination (R). 18

1.11 Example of a collision strength for Mn^{23+}. Note that the collision strength has a smooth part, corresponding to the direct excitation, and a part with resonant excitation features. The solid line (red) shows the results of our Dirac R-matrix calculations, the dashed line (blue) shows the results of our ICFT R-matrix calculations, and the squares shows the results from Aggarwal and Keenan [40]. . . 24

1.12 Overview of the R-matrix inner and outer region definitions 27

2.1 Collision strength for the a)$1s^2$ ($^1S_0$) → $1s2p(^1P_1)$ b)$1s^2$ ($^1S_0$) → $1s2s(^3S_1)$ c)$1s^2$ ($^1S_0$) → $1s2p(^3P_1)$ d)$1s^2$ ($^1S_0$) → $1s2p(^3P_2)$ transitions for Cr^{22+}. The solid line (red) shows the DARC damped calculation, the dashed line (blue) shows the ICFT damped calculation, and the results of Aggarwal and Keenan [40] are shown by solid squares. 38

2.2 Collision strength for the $1s^2$ ($^1S_0$) $\rightarrow$ 1s2s ($^1S_0$) transition for Cr^{22+}. The solid line (red) shows the DARC damped calculation and the dashed line (blue) shows the ICFT damped calculation. The results of Aggarwal and Keenan [40] are shown by solid squares. Also shown are the RCCC results (solid circle). 39

2.3 Ratio of effective collision strengths for He-like Ni for Te= 1×10^6. The ratio compares the 120k and 240k files. The green squares shows just the transitions from the ground, while the red squares shows all of the transitions in the file. . . 41

2.4 Effective collision strength for the a) $1s^2(^1S_0) \rightarrow 1s2p(^1P_1)$ b) $1s^2(^1S_0) \rightarrow 1s2s(^3S_1)$ c) $1s^2(^1S_0) \rightarrow 1s2p(^3P_1)$ d) $1s^2(^1S_0) \rightarrow 1s2p(^3P_2)$ transitions for Cr^{22+}. The solid line (red) shows the DARC damped calculation, the light blue line shows the DARC undamped calculation and the dark blue line shows the ICFT damped calculation. The results of Aggarwal and Keenan [40] are shown by solid squares. Note that in figure a) the calculations all give very similar results and cannot be resolved on the plot. 43

2.5 Effective collision strength for the $1s^2(^1S_0) \rightarrow$ 1s2s ($^1S_0$) transition for Cr^{22+}. The solid line (red) shows the DARC damped calculation and the dashed line (light blue) shows the DARC undamped calculations. The ICFT damped calculations are shown by the dark blue line. The results of Aggarwal and Keenan [40] are shown by solid squares. 44

2.6 Components of the total Kα emission for Fe^{24+}. In a) the dashed line with squares shows the total Kα PEC. The solid line shows the total PEC for the W line, the dotted line shows the total for the x line, the dot-dashed line shows the total for the y line, and the double dot-dashed line shows the PEC for the z line. 46

2.7 Ratio of the DARC to ICFT Kα PEC^{ex} (green line), and the ratio of the DARC damped to undamped Kα PEC^{ex} (red line) to show the effects of the fully relativistic method and radiation damping. 47

2.8 Kα PEC^{ex}, for Cr, Mn, and Fe as a function of electron temperature. The solid line shows the results for Cr, the dashed line shows the results for Mn and the dotted line shows the results for Mn. 48

2.9 Ratio of Fe Kα PEC^{ex} with the two-photon A-value included to the Fe Kα PEC^{ex} without the A-value included. 49

2.10 PEC^{ex} and PEC^{rec} for Fe Kα. The solid line shows the PEC^{ex} and the dashed line shows the PEC^{rec}. 50

1 Collision strength for the a)1s^2 (^{1}S$_0$) $\rightarrow$ 1s2p(^{1}P$_1$) b)1s^2 (^{1}S$_0$) $\rightarrow$ 1s2s(^{3}S$_1$) c)1s^2 (^{1}S$_0$) $\rightarrow$ 1s2p(^{3}P$_1$) d)1s^2 (^{1}S$_0$) $\rightarrow$ 1s2p(^{3}P$_2$) transitions for Mn^{23+}. The solid line (red) shows the DARC damped calculation, the dashed line (blue) shows the ICFT damped calculation, and the results of Aggarwal and Keenan [40] are shown by solid squares. 66

2 Effective collision strength for the 1s^2 (^{1}S$_0$) $\rightarrow$ 1s2s(^{1}S$_0$) transition for Mn^{23+}. The solid line (red) shows the DARC damped calculation and the dashed line shows the DARC undamped calculations. The ICFT damped calculations are shown by the dotted line (blue). The results of Aggarwal and Keenan [40] are shown by squares. 67

3 Collision strength for the a)1s^2 (^{1}S$_0$) $\rightarrow$ 1s2p(^{1}P$_1$) b)1s^2 (^{1}S$_0$) $\rightarrow$ 1s2s(^{3}S$_1$) c)1s^2 (^{1}S$_0$) $\rightarrow$ 1s2p(^{3}P$_1$) d)1s^2 (^{1}S$_0$) $\rightarrow$ 1s2p(^{3}P$_2$) transitions for Fe^{24+}. The solid line (red) shows the DARC damped calculation, the dashed line (blue) shows the ICFT damped calculation, and the results of Aggarwal and Keenan [40] are shown by solid squares. 68

4 Effective collision strength for the $1s^2$ ($^1S_0$) → $1s2s(^1S_0)$ transition for Fe^{24+}. The solid line (red) shows the DARC damped calculation and the dashed line shows the DARC undamped calculations. The ICFT damped calculations are shown by the dotted line (blue). The results of Aggarwal and Keenan [40] are shown by squares. 69

5 Effective collision strength for the a) $1s^2(^1S_0) \rightarrow 1s2p(^1P_1)$ b) $1s^2(^1S_0) \rightarrow 1s2s(^3S_1)$ c) $1s^2(^1S_0) \rightarrow 1s2p(^3P_1)$ d) $1s^2(^1S_0) \rightarrow 1s2p(^3P_2)$ transitions for Mn^{23+}. The solid line (red) shows the DARC damped calculation, the green line shows the DARC undamped calculation and the blue line shows the ICFT damped calculation. The results of Aggarwal and Keenan [40] are shown by solid squares. Note that in figure a) the calculations all give very similar results and cannot be resolved on the plot. 70

6 Effective collision strength for the $1s^2$ ($^1S_0$) → $1s2s(^1S_0)$ transition for Mn^{23+}. The solid red line shows the DARC damped calculation and the green line shows the DARC undamped calculations. The ICFT damped calculations are shown by the blue line. The results of Aggarwal and Keenan [40] are shown by squares. 71

7 Effective collision strength for the a) $1s^2(^1S_0) \rightarrow 1s2p(^1P_1)$ b) $1s^2(^1S_0) \rightarrow 1s2s(^3S_1)$ c) $1s^2(^1S_0) \rightarrow 1s2p(^3P_1)$ d) $1s^2(^1S_0) \rightarrow 1s2p(^3P_2)$ transitions for Fe^{24+}. The solid line shows the DARC damped calculation (red), the green line shows the DARC undamped calculation and the blue line shows the ICFT damped calculation. The results of Aggarwal and Keenan [40] are shown by solid squares. Note that in figure a) the calculations all give very similar results and cannot be resolved on the plot. 72

8 Effective collision strength for the 1s^2 (^{1}S$_0$) → 1s2s(^{1}S$_0$) transition for Fe^{24+}. The solid red line shows the DARC damped calculation and the green line shows the DARC undamped calculations. The ICFT damped calculations are shown by the blue line. The results of Aggarwal and Keenan [40] are shown by squares. 73

List of Tables

1.1 Spectroscopic notation for the K-α lines. 12

2.1 Level energies from NIST compared to Aggarwal (2012) [40] and present energies for Cr^{22+}. Energies are in units of Rydbergs. Differences shown as percent differences between our results and those from NIST. 32

2.2 Level energies from NIST compared to Aggarwal (2012) [40] and present energies for Mn^{23+}. Energies are in units of Rydbergs. Differences shown are percent differences between our results and those from NIST. 34

2.3 Table of radiative rates (A_{ji} in s^{-1}) for Cr XXIII transitions from the ground to the n=2 shell. 35

2.4 Table of radiative rates (A_{ji} in s^{-1}) for Mn XXIV transitions from the ground to the n=2 shell. 35

2.5 Table of two-photon A-values used for the He-like Fe-peak element ions, obtained by interpolation of the data of Derevianko and Johnson [60]. 36

3.1 Table of observed spectral line intensities for W49B, taken from [1] and [20]. Also shown in the table are the range of values of these line intensities, obtained from the fit to the spectrum. 52

3.2 Table of diagnosed H-like to He-like ratio for Fe, using the observed Lyα and Kα emission from W49B. 52

3.3 Table of diagnosed Cr and Mn abundances (relative to Fe) for W49B, using the observations of Hwang et al.[1]. 54

3.4 Table of diagnosed Cr and Mn abundances (relative to Fe) for W49B, using the observations of Ozawa et al.[20]. 54

1 Level energies from NIST compared to Aggarwal (2012) [40] and present energies for Fe^{24+}. Energies are in units of Rydbergs. Differences shown are percent differences between our results and those from NIST. Also included, is a comparison of our ICFT energy data to our DARC energy data. 62

2 Level energies from NIST compared to Aggarwal (2012) [40] and present energies for Co^{25+}. Energies are in units of Rydbergs. Differences shown are percent differences between our results and those from NIST. Also included, is a comparison of our ICFT energy data to our DARC energy data. 63

3 Level energies from NIST compared to Aggarwal (2012) [40] and present energies for Ni^{26+}. Energies are in units of Rydbergs. Differences shown are percent differences between our results and those from NIST. Also included, is a comparison of our ICFT energy data to our DARC energy data. 64

4 Table of radiative rates (A_{ji} in s^{-1}) for Fe XXV transitions from the ground to the n=2 shell. 65

5 Table of radiative rates (A_{ji} in s^{-1}) for Co XXVI transitions from the ground to the n=2 shell. 65

6 Table of radiative rates (A_{ji} in s^{-1}) for Ni XXVII transitions from the ground to the n=2 shell. 65

Chapter 1

Introduction and Background Theory

1.1 Introduction

The aim of this work is to generate high quality theoretical atomic data for use in the analysis of X-ray emission spectra of Fe-peak elements in supernova remnant (SNR) plasmas. In recent years, with the advent of space-based X-ray telescopes, the quality of X-ray spectra is sufficiently high to allow meaningful spectroscopy of these plasmas [1, 2, 3]. While the data generated in this thesis are of use for a wide range of X-ray sources, we focus, in particular, on supernova remnant plasmas due to their importance in understanding the elemental abundances of the universe. Thus, we first give an overview of supernovae and supernova remnant plasmas, before going into the details of the new work performed as part of this research.

1.1.1 Supernovae and Supernova Remnants

Supernovae are extremely energetic, though short-lived stellar events. These explosive episodes are classified according to their spectra. The spectra of Type I supernovae are characterized by a lack of hydrogen absorption lines, while Type II supernovae display hydrogen lines during at least part of the event. These categories are further subdivided according to other features of the spectra, and the manner in which the spectra change over time. An examination of these different spectra has allowed a determination of the causes of supernovae. Type Ia supernovae are thermal in nature, typically caused by the accretion of material onto a white dwarf star until it reaches the Chandrasekhar limit, approximately 1.4 solar masses. At this mass, fusion is triggered in the star, which had previously been supported against gravity by electron degeneracy pressure. The runaway fusion of carbon and oxygen triggers

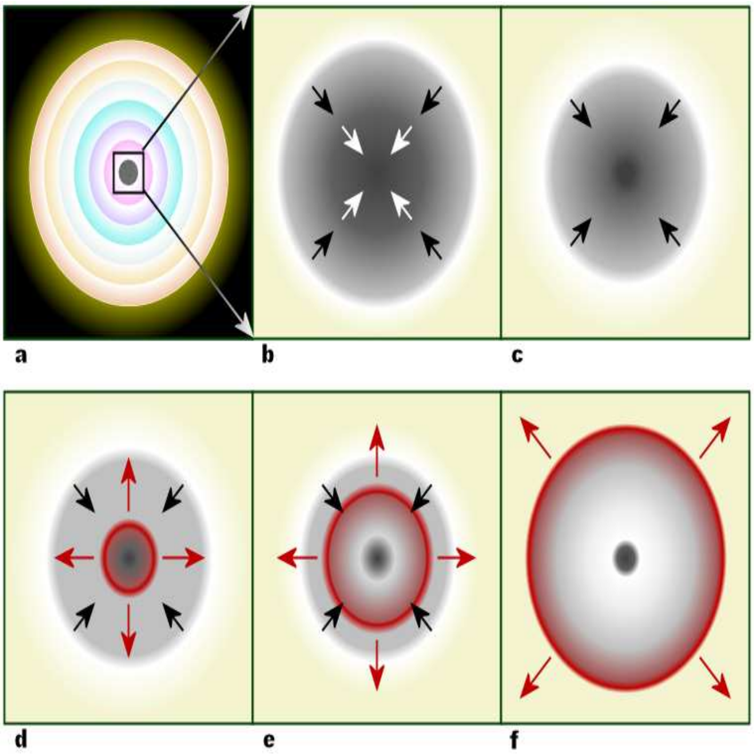

Figure 1.1: Schematic of a core-collapse supernova explosion. Figure a) shows fusion of elements in a massive star. Figure b) shows the core when it reaches the Chandrasekhar-mass and starts to collapse. In figure c) the inner core compresses into neutrons and the gravitational energy is converted into neutrinos. Figure d) shows the outward-propagating shock wave (red). (e) The shock begins to stall as nuclear processes drain energy away, but it is re-invigorated by interaction with neutrinos. (f) The material outside the inner core is ejected, leaving behind only a degenerate remnant. Illustration by R.J. Hall [GFDL (http://www.gnu.org/copyleft/fdl.html), CC-BY-SA-3.0.

an enormous explosion, resulting in the complete destruction of the star. Figure 1.1 shows the formation mechanism for a supernova.

All other supernovae occur in very massive stars. Throughout their lives, these stars are supported against gravity by the thermal pressure created by nuclear fusion. As the star's core exhausts its supply of hydrogen, it will contract until the thermal conditions are met to begin burning another element, returning the star to equilibrium. However, this process provides diminishing returns, and eventually the star will be unable to support its mass against gravity. When this happens, generally after the star has an iron core with mass greater than the Chandrasekhar limit, the core of the star collapses. The outer layers of the core may reach speeds of 70,000 km/s as it collapses. When the core has reached the density of an atomic nucleus, neutron degeneracy pressure will halt the collapse, producing a shock wave radiating outward. Due to the very high temperature of the core at this time, large numbers of neutrinos are emitted. These neutrinos are re-absorbed by the outer layers of the core, producing a massive explosion. Depending on the size of the progenitor star, the core may form a neutron star or a black hole.

While these events are spectacular, and scientifically very interesting, they are of a very brief duration, lasting only days to weeks. They are also relatively rare, occurring approximately once every fifty years in the Milky Way. This provides limited opportunity to observe these phenomena. However, supernova remnants are much longer lived, which allows ample opportunity to observe them. SNRs comprise material ejected from supernova explosions. By examining spectra of these remnants, a great deal can be determined about both the progenitor star and the supernova process. These processes are thought to have important impacts on the galaxy as a whole by enriching the interstellar medium with heavy elements, and possible heating of the interstellar medium. They are thought to play a significant role in star formation processes.

Type Ia supernovae have proven to be fascinating objects and their spectra are used in a wide range of astrophysical applications. They are believed to arise from thermonuclear explosions of low-mass stars such as a white dwarf which accretes material from a companion star until the progenitor's mass crosses the Chandrasekhar limit [4]. Due to their characteristic light curve, they have been used as standard candles [5], providing a useful distance measurement to red-shifted galaxies [6]. As such, Type Ia supernova spectra have been used to determine the Hubble constant [7] and, in more recent years, to measure the acceleration of the universe [8]. Modeling Type Ia supernova nucleosynthesis is key in understanding the elemental abundances in the universe. Type Ia supernovae are also believed to play a significant role in the heating of the interstellar medium [9] and may be responsible for a significant fraction of the loss of material from galaxies [10]. Questions have been raised

[11] pointing out the possibility that Type Ia supernovae may undergo sub-Chandrasekhar explosions [12], thus questioning their use as standard candles. This highlights one of the main outstanding issues in supernova research, namely that we have a limited understanding of the progenitor stars.

The material ejected during the supernova explosion quickly undergoes adiabatic cooling. There is a reverse shock wave that propagates in the opposite direction to the exploding material (in the reference frame of the ejecta), and this collision-less shock is responsible for the heating of the supernova remnant plasma. The shock wave efficiently heats the electrons (up to a few keV), while the ions remain relatively cool. The evolution of the spectra from the SNR plasma is then a reflection of the free electrons gradually redistributing their energy to the plasma ions. Thus, while the ions start in low charge states, they gradually ionize to H- and He-like ions in most SNR plasmas. However, this can take up to tens of thousands of years so many SNR plasma are not in ionization equilibrium. This is often referred to as non-equilibrium ionization (NEI).

Consider Figure 1.2, which shows a time-dependent ionization balance of Fe for a SNR plasma with electron density of 10 cm^{-3} and an electron temperature of 2 keV. Note that this is similar to the conditions for the SNR plasma W49B. Note that it takes a little over 1000 years for the plasma to reach equilibrium. There is, however, an open question as to whether W49B is indeed in ionization equilibrium. We will return to this in chapter 3. It can also be seen that at these electron temperatures, one would expect mostly He-like Fe once the SNR reaches ionization equilibrium.

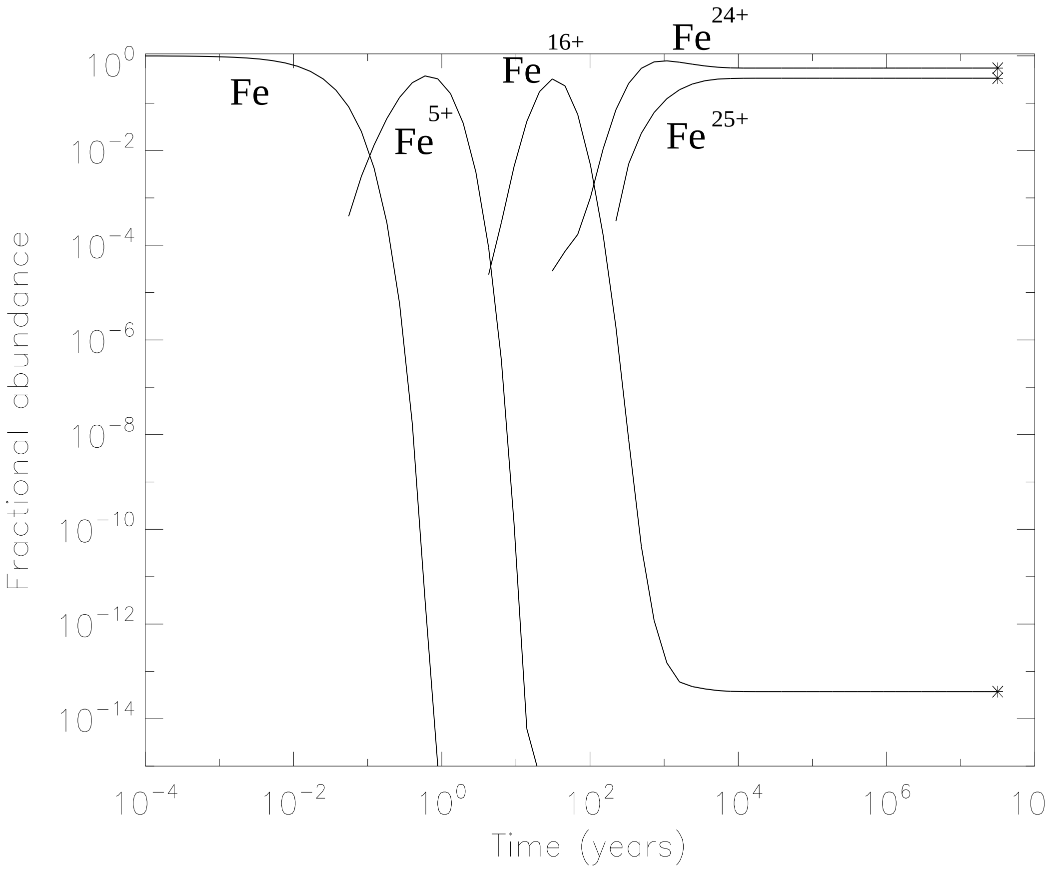

Figure 1.2: Time-dependent ionization balance for Fe. The Fe ions are assumed to start as neutral and the electron temperature and density are kept constant (N_e=10 cm^{-3} and T_e=2 keV). Note that for clarity only, selected ion stages are shown in the plot. The stars show the equilibrium fractional abundances for the He-like and H-like ion stages for a 2 keV plasma.

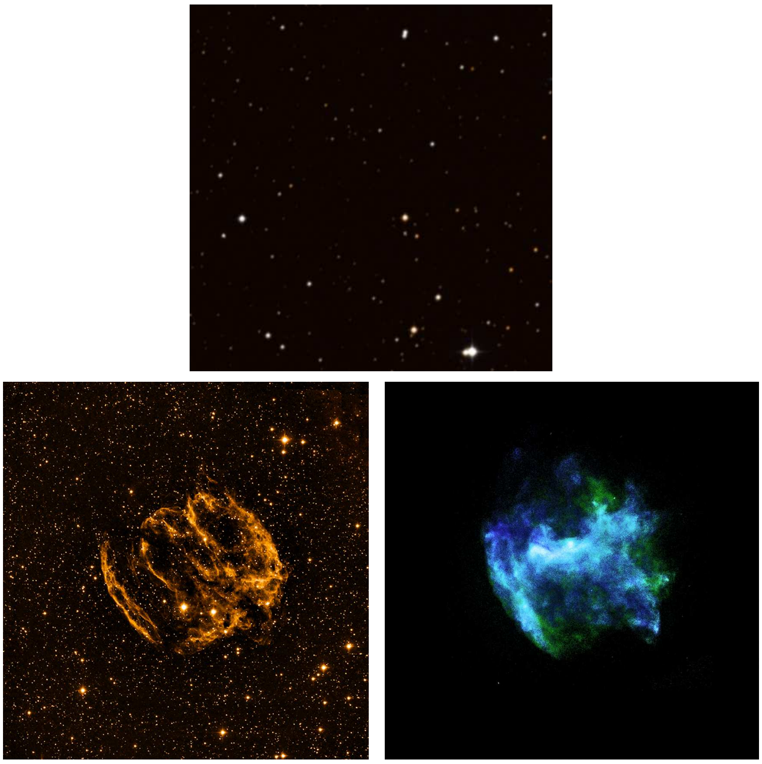

Figure 1.3: Images of W49B. The top figure shows the Digitized Sky Survey (DSS) optical image, the bottom left shows the infra-red image, and the bottom right hand image shows the X-ray image. Note that they are all in the same field of view.

1.1.2 Observations of supernova remnants

When one observes a SNR plasma from hundreds to thousands of years after the explosion, there is very little visible radiation detected, see Figures 1.3 and 1.4 for examples of W49B and Cassiopeia A (Cas A) respectively. However, one does observe a strong X-ray signature, see Figures 1.3 and 1.5. The supernova remnant (Cas A), located 11,000 light-years away in our own galaxy, is the result of the explosion of a massive star some 300 years ago. It is considered to be the strongest radio source in the sky beyond our solar system and the youngest of the SNRs in our galaxy.

The Galactic supernova remnant W49B is a particularly interesting object. In this thesis, we make use of our new atomic data in order to analyze certain aspects of W49B (and other SNR plasmas like it). See Fig 1.3 for the images of W49B at different wavelengths. Note that W49B cannot be seen in the visible, due to the time since the explosion and the high temperatures that remain. First observed in X-rays by the Einstein Observatory [13], Fe line emission was later detected by EXOSAT [14]. The SNR shows a shell like shape at radio wavelengths, with the X-ray emission coming largely from the core region. While Fujimoto et al. [15] suggested that the elements were stratified, Hwang et al. [1] showed that the spectra could also be explained by a two temperature model. Note that SNR plasmas with center filled morphologies, such as W49B, are rare, making W49B of considerable interest. It is believed to lie about 26,000 light years away [16] and the supernova explosion happened about 1000 years ago. The electron density is believed to be about 10 cm^{-3} [15], which is relatively high for a supernova remnant plasma. Hwang et al. [1] put a lower limit on the electron density of 2 cm^{-3}, stating that the true density could be significantly higher.

Figure 1.6 shows the X-ray spectrum of W49B, taken using XMM-Newton (figure taken from Miceli et al. [2]). Note the presence of mostly H-like and He-like spectral lines, along with the weak features due to Cr and Mn between 5 and 6 keV. Figure 1.7 shows the ASCA spectrum [1] of the Cr and Mn features. Note that each ion produces a single spectral feature, and that their energies agree well with those expected from He-like Cr and He-like Mn.

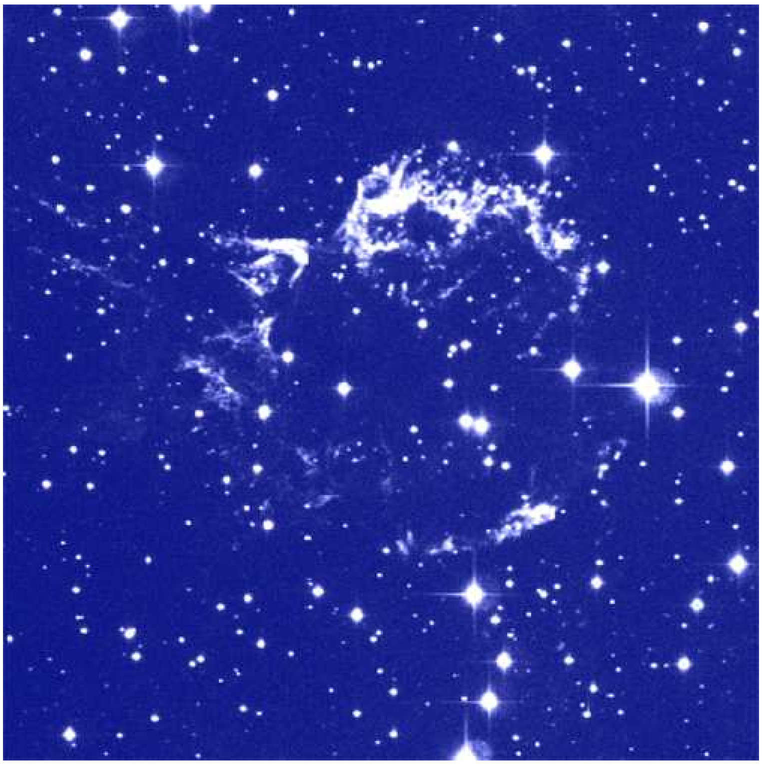

Figure 1.4: Supernova remnant Cassiopeia (Cas A) at optical wavelength.

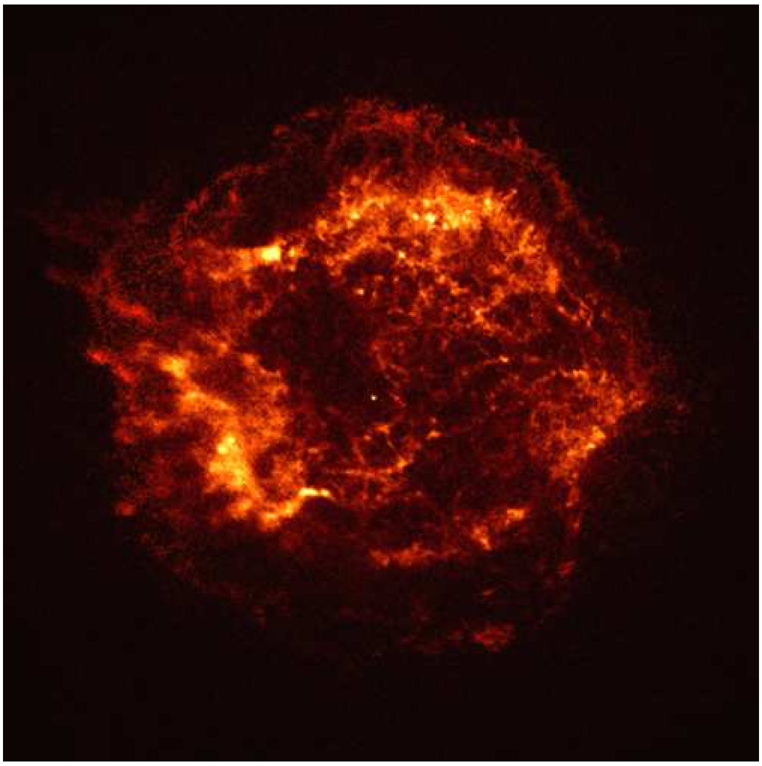

Figure 1.5: CHANDRA X-ray image of supernova remnant Cas A.

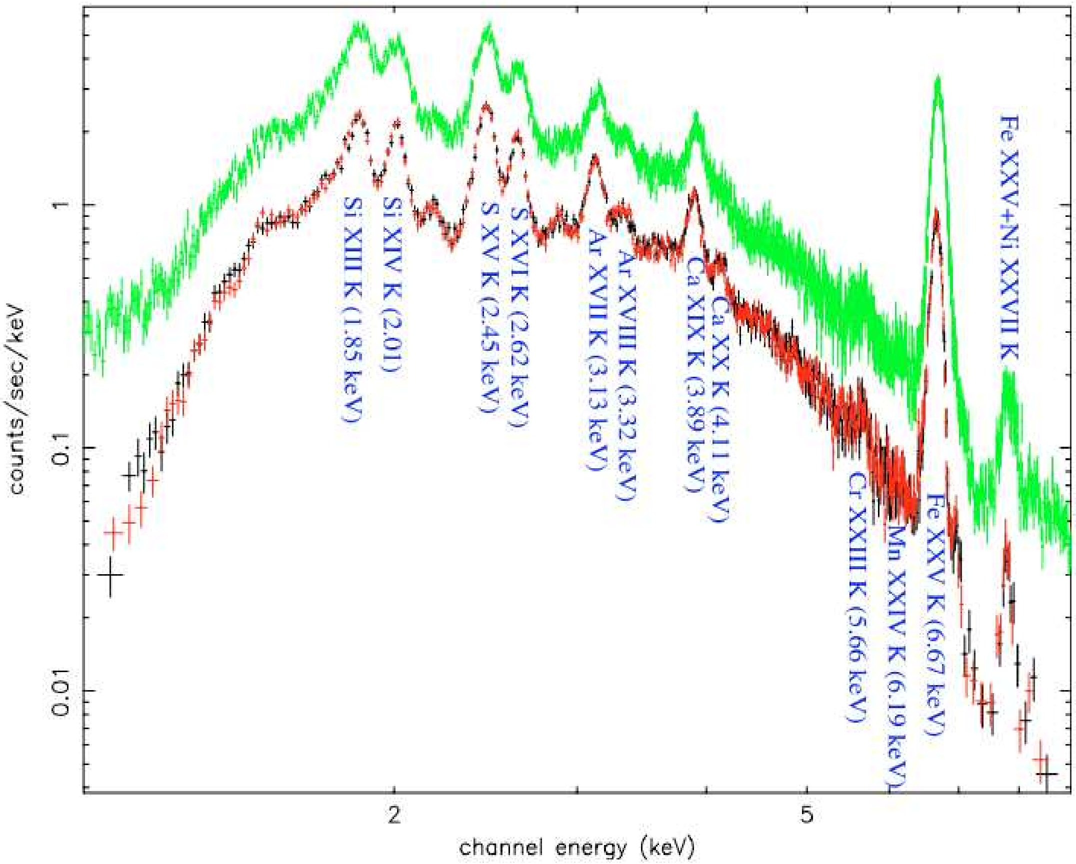

Figure 1.6: X-ray spectrum of W49B, taken from Miceli et al. [2]. The two different spectra are the results from the two spectrometers on the XMM-Newton telescope. The spectral lines are identified in the figure, while the strong background continuum is due to thermal Bremsstrahlung radiation.

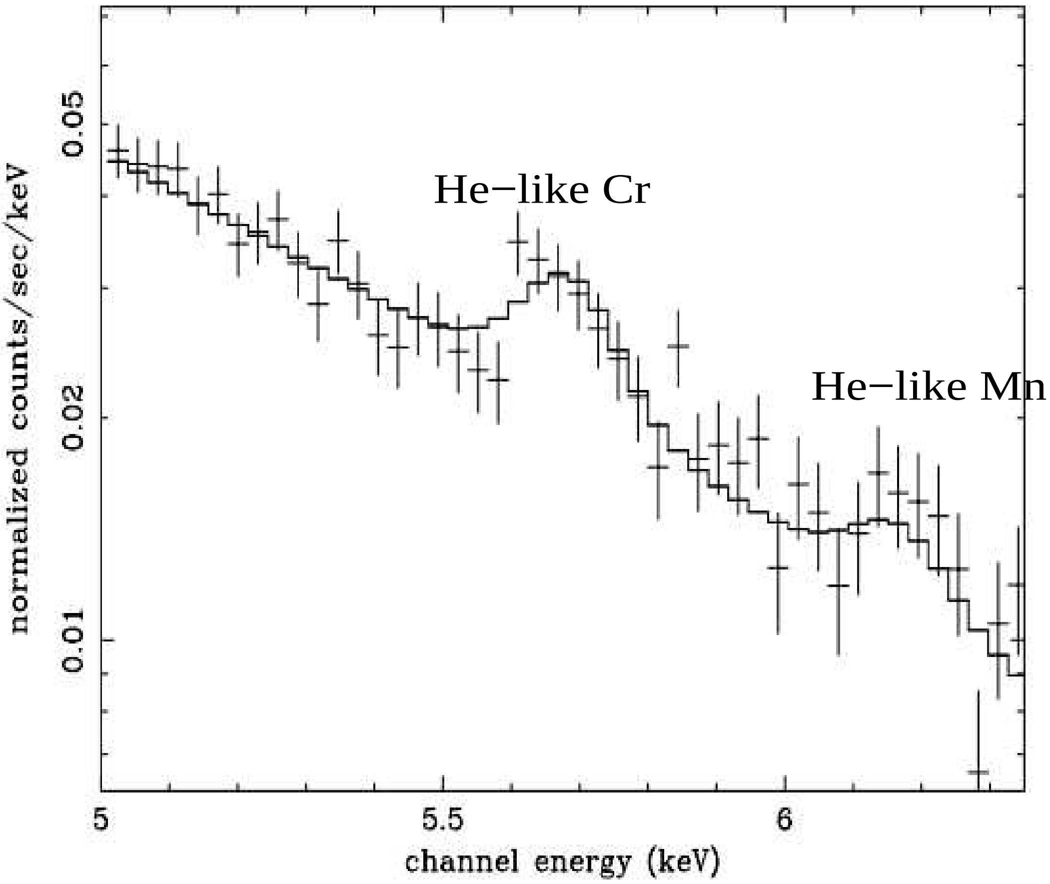

Figure 1.7: The Cr and Mn X-ray spectral features of W49B, taken from [1]. The first spectral line is of He-like Cr while the second is of He-like Mn.

While the He-like spectral feature for each ion is observed as a single peak, it consists of four unresolved spectral lines. Figure 1.8 shows a Grotrian diagram for He-like systems. The four spectral lines that make up the He-like Kα features are the indicated w, x, y, and z lines. These are described in Table 1.1, we will be using this notation in later chapters. Note that there is one other transition shown in Figure 1.8, the 1s2s(^{1}S$_0$) → 1s^2 (^{1}S$_0$) transition. This is only allowed through a two-photon transition and as such, has a very small rate coefficient. For this transition, two photons are emitted simultaneously, but with energies that add up to the difference in the bound state energies. As a result, this transition does not contribute photons to the Kα spectral feature. However, as will be shown later, it is important for the population modeling as it is the main radiative decay route for the 1s2s(^{1}S$_0$) level.

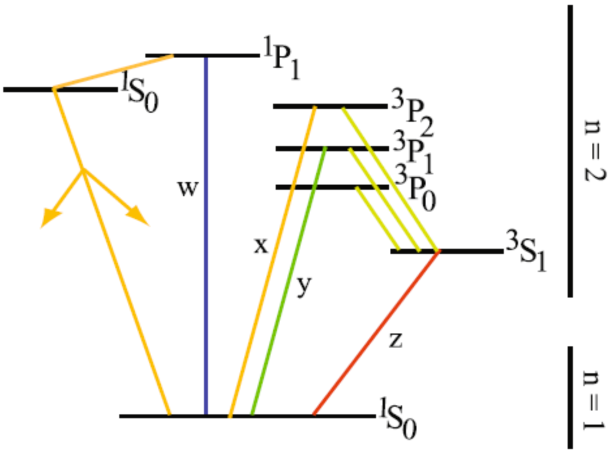

Figure 1.8: Grotrian diagram for He-like systems, showing the spontaneous emission transitions.

Table 1.1: Spectroscopic notation for the K-α lines.

Transition	Letter notation
$1s2s(^3S_1) \rightarrow 1s^2\ (^1S_0)$	z
$1s2p(^3P_1) \rightarrow 1s^2\ (^1S_0)$	y
$1s2p(^3P_2) \rightarrow 1s^2\ (^1S_0)$	x
$1s2p(^1P_1) \rightarrow 1s^2\ (^1S_0)$	w

1.1.3 Previous X-Ray Observations of Cr and Mn

In recent years, a number of X-ray observations of weak spectral emission from the less abundant Fe-peak elements (Mn, Cr, and Ni) have been made from a range of astrophysical sources. These include observations of emission of He-like Mn and Cr from the W49B supernova remnant using ASCA [15, 1] and XMM-Newton [2], and observations of Ne-like Mn and Cr emission from the Tycho supernova remnant using Suzaku [17]. Cr emission has also been observed from a number of supernova remnant plasmas using Chandra [18], finding that the Cr and Fe ions are likely to be co-located in the SNR plasmas. This was confirmed in a later study [3], and the ratio of the equivalent widths for the Cr and Fe emission was used to put constraints on the SNR progenitor. Park et al. [19] used Mn-to-Cr line ratios to show that the progenitor of Kepler's supernova has a super-solar metallicity. Ozawa et al. [20] detected Cr and Mn from W49B, as well as detected a strong radiative recombination feature of Fe. They also showed that the plasma is overionized, i.e. the elements have a higher charge state than one would expect in collisional-ionization equilibrium (CIE), where the equilibrium conditions are evaluated for the electron temperature that is measured using the slope of the continuum.

In general, the X-ray observations of Cr and Mn emission cluster into two categories. In the first, case the emission is dominantly from ion stages close to the He-like ion stages (e.g. W49B, see [1, 3]), and in the second, the emission is from ion stages close to the Ne-like ion stages (e.g. Tycho, see [17]). However, a lack of accurate atomic data has hampered the use of Kα spectral lines in diagnostics studies. Hwang et al. [1] interpolated the photon emissivity

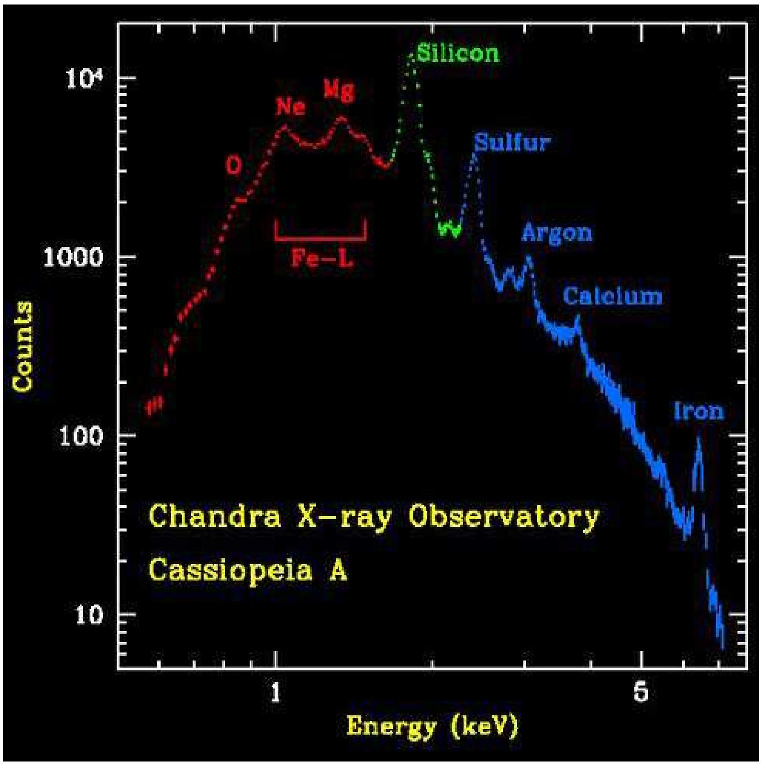

Figure 1.9: X-ray spectra of Cas A, taken using the CHANDRA X-ray observatory.

coefficient data of Raymond and Smith [21] to determine approximate abundances of Mn and Cr in W49B. XSPEC (`http://heasarc.gsfc.nasa.gov/xanadu/xspec/`), a commonly used spectral fitting program, currently does not have emission data for Cr or Mn. New data for use in SNR studies are starting to be generated, such as the distorted-wave data generated using the Flexible Atomic Code [22] that was then used in their analysis of Kepler's supernova remnant plasma.

A number of important questions about W49B (and other SNR plasmas) can be answered once accurate atomic data exist for Cr and Mn. There is currently a debate whether W49B is overionized or not, i.e. do the elements have a higher charge state than one would expect from collisional ionization equilibrium. Hwang et al. [1] found that the X-ray spectrum of W49B was close to CIE. Kawasaki et al. [23], also using ASCA observations, found evidence for overionization when modeling Ar and Ca spectra. Miceli et al. [2], using XMM-Newton spectra of the central region of W49B found no evidence of overionization. Recently, Ozawa et al. [20] detected a strong radiative recombination continuum of Fe in W49B, and showed that one must consider the recombination contributions to He-like Fe when modeling the Kα spectra of Fe^{24+}. They also find the plasma to be overionized.

Another question under debate for W49B is the nature of the supernova explosion. Using abundance diagnostics, Hwang et al. [1] suggested that it is a Type Ia SN. However, with better constraints on the Fe-peak element abundances, this could be determined with more confidence.

While there are now many observations of Kα emission from SNR plasmas, very little work has been done determining Cr, Mn, and Ni abundances from the observations, or testing the quality of the atomic data required for such diagnostics. The purpose of this thesis is to generate high quality atomic data for He-like Fe-peak elements, testing their effect on emissivities. We use spectra of W49B to illustrate how the new data can be used, both for fractional abundances within an element, and for elemental abundances. As part of this study, we wish to determine what physical effects have to be included in the electron-impact excitation data, and their influence on the total Kα emission. It was recently demonstrated [24] that for H-like Fe-peak elements, fully relativistic effects resulted in effective collision strengths that were about 10% higher than semi-relativistic collision strengths. Radiation damping was also found to affect the effective collision strengths below a temperature of about 200 eV. Radiation damping will be described in section 1.3. In this thesis we wish to determine whether these effects have to be included for the He-like Fe-peak element ions. This will help guide future calculations for the remaining ions of the Fe-peak elements. We note that the new data generated in this work consists of electron-impact excitation/de-excitation rate coefficients, along with spontaneous emission coefficients. This data is then combined with recombination data for free electrons recombining with the H-like ions, to produce a final dataset for each ion. The new atomic data is used in a collisional-radiative code [25] to generate photon emissivity coefficients as a function of electron temperature and density for the Fe-peak element He-like ions. We use the photon emissivities to diagnose elemental abundances for Mn and Cr in supernova remnant plasmas.

In this work, we also address a number of the aforementioned questions about SNR W49B. Using new data for He-like Fe, along with existing data for H-like Fe, we will determine the fractional abundance of these ion stages in W49B. This will address the question of overionization, and determine whether the presence of the H-like ion stage affects the He-like line intensities as suggested by Ozawa et al. [20]. We then use the new data for the He-like ions to determine accurate elemental abundances of Cr and Mn in W49B. This information can then be used to address questions on the explosion mechanism in the supernova.

1.1.4 Overview of atomic data for He-like Fe-peak elements

We first present a brief review of the atomic data on the Fe-peak elements. Due to the relatively strong emission from He-like Fe in X-ray astrophysical sources, much previous work has focused on this ion. Only a small number of studies have been undertaken measuring the experimental collision cross sections. There are also a smaller number of previous papers on atomic data for He-like Cr, Mn, Co and Ni. Excitation cross sections for He-like Fe and Ni were measured by Thorn et al. [26] between energies of 35 and 85 keV. Experimental measurements of the electron-impact excitation cross sections that populate the upper levels of the w, x, y, and z transitions in He-like Ti, Cr, Mn and Fe were performed by Wong et al. [27] at high energies (6.8 keV for Fe^{24+}).

For the electron-impact excitation theoretical atomic data for He-like Fe, a wide range of calculations have been performed. The following provides an overview of the various collisional approaches adopted for He-like Fe over the last few decades. These include Coulomb-Born approximation results [28] and distorted-wave calculations [29, 30]. Zhang et al. [29] included the effects of resonances and radiation damping in their calculations. Pradhan et al. [31, 32] used a multi-channel quantum defect theory and a combined close-coupling and distorted-wave approach in calculations for Fe^{24+}. Pradhan et al. [33] compiled a set of

Maxwellian rate coefficients for He-like Ca and Fe using the collision strengths from previous papers.

Keenan et al. [34] estimated He-like Mn excitation rate coefficients from interpolation of R-matrix calculations of other He-like ions. Zhang et al. [35] used the Breit-Pauli R-matrix codes for B-like and He-like Fe, with the effects of radiation damping included. Kimura et al. [36] calculated Dirac R-matrix collision strengths for He-like S, Ca and Fe for the lowest 31 target levels. Whiteford et al. [37] calculated R-matrix level-resolved excitation data using the intermediate-coupling frame-transformation (ICFT) method [38]. They evaluate excitation data between the levels of the first five n-shells of He-like Fe and include the effects of radiation damping. In 2009, Griffin and Ballance [39] calculated Dirac R-matrix excitation data up to n=5 for He-like Fe, including the effects of radiation damping. It was found that radiation damping has a substantial effect on the effective collision strengths at the lowest temperatures. In their paper, they also describe the effects of radiation damping on the angular distribution of the scattered electrons.

In 2012, Aggarwal and Keenan published their work on electron impact excitation rates for He-like ions such as Ti, V, Cr, and Mn [40]. They calculated these rates up to approximately 2.7 keV. In a 2013 publication [41], they report on a similar study done for He-like Fe, Co, Ni, Cu, and Zn in which rates were calculated up to approximately 4.3 keV. Both studies were carried out by using relativistic R-matrix codes without radiation damping. In this work we compare mostly with these calculations.

1.1.5 Fe-Peak Elements for Use in Diagnostics

The potential use of Fe-peak element spectra has been widely demonstrated, though as yet, has not been used in practice due to the lack of atomic data. For example, one can determine the metallicity of supernova progenitors using the Mn-to-Co spectral line ratio, as demonstrated by Badenes et al. [42]. Yang et al. [18] showed that the ratio of the equivalent line widths of Cr-to-Fe can contain information about the progenitor and the explosion mechanism. They showed that this method has the potential to constrain detonation models for Type Ia events. Also, line ratios from the He-like or Ne-like ion stages are temperature sensitive [43].

1.2 Spectral Modeling

1.2.1 Collisional Radiative Modeling and Photon Emissivity Coefficients

The new atomic data is used in a collisional-radiative model to evaluate photon emissivities, which are then used to interpret the X-ray spectra of SNR W49B . In this thesis, we focus on diagnosing fractional and elemental abundances of the Fe-peak elements. The fractional abundances give the amount of each ion stage that is present for an element, while the elemental abundances give the amount of a given element relative to another (e.g. the ratio of Cr to Fe). In our calculations, we use the Atomic Data and Analysis Structure (ADAS) suite of codes [25]. This approach is based on collisional-radiative theory as developed by Bates et al. [44], which was later generalized by Summers et al. [25]. Note that for this study, we will be modeling the emission of the H-like and He-like ion stages of the Fe-peak elements.

Consider the level populations for level j and all of the mechanisms that can populate and depopulate it. Figure 1.10 shows a schematic illustrating the main processes.

One can set up an equation accounting for the rate of change of population into a level j, balancing all of the processes mentioned in the figure caption:

$$\begin{aligned} \frac{dN_j}{dt} &= \sum_{i<j} N_i N_e q_{i\to j} + \sum_{k>j} N_k (N_e q_{k\to j} + A_{k\to j}) \\ & -N_j (\sum_{i<j} (N_e q_{j\to i} + A_{j\to i}) + \sum_{k>j} N_e q_{j\to k} + N_e S_j) + N_e N_1^+ R_j \ , \end{aligned} \tag{1.1}$$

with a similar equation for each of the excited levels, resulting in a set of simultaneous equations that can be expressed in matrix form.

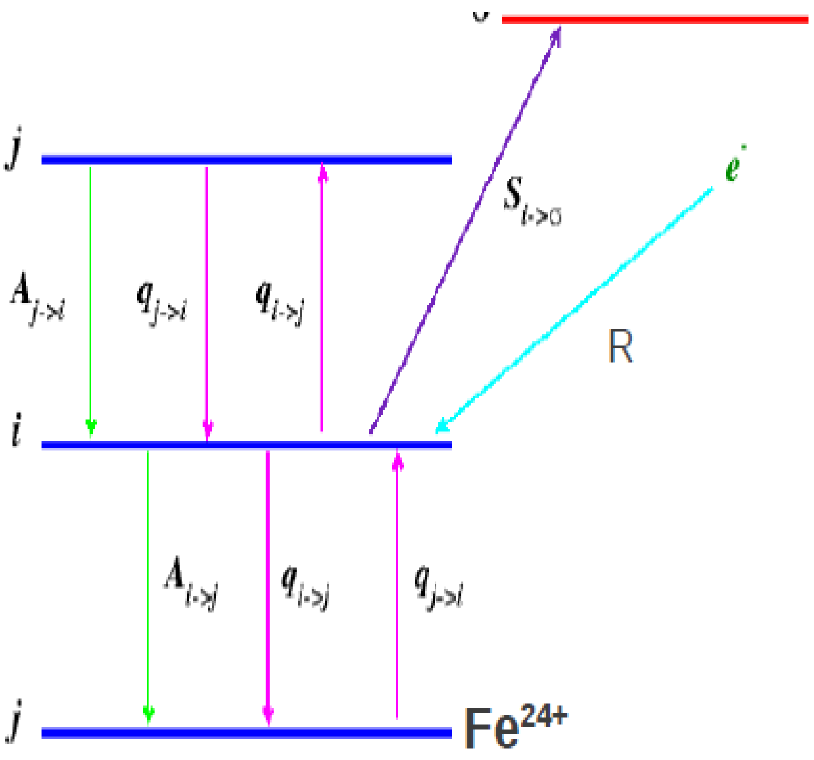

Figure 1.10: Schematic showing the mechanisms for populating and depopulating a level in Fe^{24+}. The processes include spontaneous emission ($A_{i \to j}$), electron-impact excitation and de-excitation (q), electron-impact ionization (S) and electron-recombination (R).

Here, N_j is the population number density of excited level j, and N_e is the free electron density. S_j is the ionization rate coefficient from excited term j to the next ion stage, and R_j is the recombination rate coefficient from the ground level of the next ion stage (with population N_1^+) to the excited term j. $A_{i \to j}$ is the spontaneous emission rate from level i to level j. The q values represent electron-impact collisional excitation and de-excitation rate coefficients between the bound levels.

For the He-like ions considered in this thesis, we evaluate all of the q-values from the R-matrix effective collision strengths. The A-values are also calculated as part of this work. The recombination rate coefficients consist of radiative and dielectronic recombination, both of which have been calculated previously for these ions. For the cases considered here, ionization losses from the excited levels are negligible and do not need to be included in the modeling. The electron density required for excited state ionization to become important for these ions is far greater than the values for SNR plasmas.

The rate equations can be reduced to a more compact form where one separates the transitions within the ion stage from those due to recombination from the next ion stage:

$$\frac{dN_j}{dt} = N_e N_1^+ R_j + \sum_i C_{ji} N_i \tag{1.2}$$

where C is the collisional radiative matrix. If $i < j$

$$C_{ji} = A_{i \to j} + N_e q_{i \to j} \tag{1.3}$$

and if $i = j$,

$$C_{ii} = -\Big(\sum_{i>j} A_{i \to j} + N_e \sum_{j \neq i} q_{i \to j} + N_e S_i \Big) \tag{1.4}$$

Note that the recombination rate coefficient consists of three contributions, namely radiative, dielectronic and three-body recombination ($R_j = \alpha_j^r + \alpha_j^d + N_e \alpha_j^3$). The equation can thus be written as

$$\sum_j C_{ij} N_j = \frac{dN_j}{dt} - n_e N_1^+ R_j \tag{1.5}$$

The ground and metastable states vary on a slow timescale (driven by ionization and recombination collision times), and thus they must be evaluated as part of a non-equilibrium ionization balance (or inferred from the spectral measurements). This is particularly true for SNR plasmas where the ions take very long times to reach equilibrium. One of the open questions about SNR W49B is whether it is in ionization equilibrium, and we investigate this in Section 4. The excited states, on the other hand, very quickly come into equilibrium due to their large radiative rates, and one can set their dN/dt values to zero. Thus, the population of the j^{th} ‘ordinary’ level can be solved for the contribution due to each of the ‘driving’ populations. Thus, the ground and metastable populations are left as unknowns.

$$N_j^z = -\sum_i C^{-1}_{ji_{(r)}} C_{i1} N_1^z - \sum_i C^{-1}_{ji_{(r)}} R_i N_1^+ n_e \tag{1.6}$$

where $C^{-1}_{ji_{(r)}}$ is the reduced collisional radiative matrix that has had the ground and metastable rows/columns removed.

The set of equations given by Eqn. 1.6 can be written in matrix form and solved for the excited populations. It is common to separate the ionization balance calculation from the excited population calculation. The ground and metastable populations for each ion stage can be calculated as part of a time-dependent ionization balance calculation, or as in the case of the present study, it can be inferred from the spectrum.

Thus, the excited level population is evaluated in terms of these ‘driving’ ground and metastable populations. The He-like ions have potential metastable levels that cannot decay to the ground via an electric dipole transition. However, the lifetimes of these levels are still much shorter than the SNR plasma timescales, so they can be considered to be in equilibrium with the ground level. Thus, the excited populations of the He-like ions are given by:

$$N_j = (F^{ex}_{1s^2\,(^1S)}) N_e N^{He-like}_{1s^2\,(^1S)} + (F^{rec}_{1s\,(^2S)}) N_e N^{H-like}_{1s\,(^2S)} \tag{1.7}$$

where $F^{ex}_{1s^2\,(^1S)}$ is the contribution to the excited level j due to excitation and collisional-redistribution within the He-like ion stage, and $F^{rec}_{1s\,(^2S)}$ is the contribution due to recombination from the H-like stage, followed by collisional and radiative redistribution within the He-like ion stage. The F-values consist of collisional and radiative rates and are evaluated by solving the collisional-radiative equations. These coefficients are a function of both electron temperature and density, see [25] for further details on these F-coefficients.

One can then take these excited populations and evaluate photon emissivity coefficients (PECs), for use in spectral diagnostics. The photon emissivity for a given transition $j \rightarrow k$, can be split into 'excitation' and 'recombination' contributions in a similar way to the excited populations. Thus, the line intensity in a spectral transition would be given by

$$I_{j\to k} = (PEC^{exc}_{j\to k})N_e \left(\frac{N^{He-like}_{1s^2\,(^1S)}}{N^{TOT}}\right) N^{TOT} + (PEC^{rec}_{j\to k})N_e \left(\frac{N^{H-like}_{1s\,(^2S)}}{N^{TOT}}\right) N^{TOT} \quad (1.8)$$

where

$$\begin{aligned} PEC^{exc}_{j\to k} &= A_{j\to k}F^{ex}_{1s^2\,(^1S)} & (1.9)\\ PEC^{rec}_{j\to k} &= A_{j\to k}F^{rec}_{1s\,(^2S)} & (1.10) \end{aligned}$$

and N^{TOT} is the total number of atoms/ions per unit volume in the plasma. Note that these PEC coefficients are a function of electron temperature and density and are easily archived for use in the modeling. In the analysis of the He-like Kα and the H-like Lyα spectral features shown later in this thesis, we construct a total Kα PEC and a total Lyα PEC consisting of a sum over the contributing spectral lines.

The spectral observations of W49B shows evidence of H-like Fe (e.g. in the recombination continuum observed at $\sim$ 9 keV and in the Fe Lyα spectral feature at 6.9 keV). Thus, in the interpretation of the He-like spectral features it is important to know if the recombination contribution to the line emission is important. That is, does one need to include a PEC^{rec} in the spectral modeling? This depends upon the fraction of the H-like ion that is present in the plasma, which can be determined from a comparison of the observed spectra from the He-like and H-like ion stages.

1.2.2 Diagnostics of Fractional and Elemental Abundances

Before determining the elemental abundances of Cr and Mn in the SNR plasmas, one must determine whether the H-like ion stages of these ions provide a significant populating mechanism for the He-like ion excited states and must be considered in the modeling. Unfortunately, the only observed emission from Cr and Mn is from the He-like ion stages. On the other hand, one observes lines from both H-like and He-like Fe, and we know that Cr and Mn are co-located with the Fe emission [18]. Thus, it is possible to use the observed Fe emission, along with theoretical data for the H-like and He-like ion stages, to determine the fraction of Fe in the H-like ion stage. This can be used to check if one needs to include a recombination contribution to the He-like spectral emission. It can then be assumed that the Cr and Mn ion stages have the same fraction of H-like to He-like ions present as Fe. This fraction can then be used when evaluating the Cr and Mn elemental abundances.

Consider the line ratio of the Fe^{25+} Lyα transition to the Fe^{24+} Kα transition. While one needs to consider a recombination contribution to the He-like Kα feature, it seems unlikely that there is enough bare Fe nuclei present to require a PEC^{rec} contribution to the Lyα feature. As will be seen later, the H-like ions are less than 10% of the He-like abundance, so it is reasonable to assume that there is little Fe^{26+} present in the plasma. The line ratio of Lyα to Kα is given by:

$$\frac{I_{Ly\alpha}^{Fe^{25+}}}{I_{K\alpha}^{Fe^{24+}}} = \frac{PEC_{Ly\alpha}^{ex}\left(\frac{N^{Fe^{25+}}}{N^{Fe_{TOT}}}\right)N^{Fe_{TOT}}}{PEC_{K\alpha}^{ex}\left(\frac{N^{Fe^{24+}}}{N^{Fe_{TOT}}}\right)N^{Fe_{TOT}} + PEC_{K\alpha}^{rec}\left(\frac{N^{Fe^{25+}}}{N^{Fe_{TOT}}}\right)N^{Fe_{TOT}}} \tag{1.11}$$

This can be solved to give

$$\frac{N^{Fe^{25+}}}{N^{Fe^{24+}}} = \frac{PEC_{K\alpha}^{ex}}{PEC_{Ly\alpha}\left(\frac{I_{K\alpha}^{Fe^{25+}}}{I_{Ly\alpha}^{Fe^{24+}}}\right) - PEC_{K\alpha}^{rec}} \tag{1.12}$$

One can use an observation of the observed Lyα and Kα intensities, along with theoretical values for the PEC coefficients, to determine the relative abundance of the H-like to the He-like ion stages for Fe.

Once one knows the fractional abundance for H-like and He-like Fe, and assuming that it is very similar to the Cr and Mn fractional abundances, one can determine the elemental abundance of Cr and Mn. The line ratio of the He-like Kα transition in Cr to the He-like

Kα transition in Fe is given by

$$\frac{I_{K\alpha}^{Cr^{22+}}}{I_{K\alpha}^{Fe^{24+}}} = \left(\frac{PEC_{CrK\alpha}^{ex}\left(\frac{N^{Cr^{22+}}}{N^{Cr_{TOT}}}\right) + PEC_{CrK\alpha}^{rec}\left(\frac{N^{Cr^{23+}}}{N^{Cr_{TOT}}}\right)}{PEC_{FeK\alpha}^{ex}\left(\frac{N^{Fe^{24+}}}{N^{Fe_{TOT}}}\right) + PEC_{FeK\alpha}^{rec}\left(\frac{N^{Fe^{25+}}}{N^{Fe_{TOT}}}\right)} \right) \left(\frac{N^{Cr_{TOT}}}{N^{Fe_{TOT}}} \right) \tag{1.13}$$

Assuming that $N^{Cr22+}/N^{Cr_{TOT}} = N^{Fe24+}/N^{Fe_{TOT}}$ and $N^{Cr23+}/N^{Cr_{TOT}} = N^{Fe25+}/N^{Fe_{TOT}}$, one can determine the ratio of Cr-to-Fe abundance given an observed Kα emission for both ions. The same method can be used to get the Mn relative abundance.

$$\frac{N^{Cr_{TOT}}}{N^{Fe_{TOT}}} = \left(\frac{I_{K\alpha}^{Cr^{22+}}}{I_{K\alpha}^{Fe^{24+}}} \right) \left(\frac{PEC_{CrK\alpha}^{ex} + PEC_{CrK\alpha}^{rec}\left(\frac{N^{Fe^{25+}}}{N^{Fe^{24+}}}\right)}{PEC_{FeK\alpha}^{ex} + PEC_{FeK\alpha}^{rec}\left(\frac{N^{Fe^{25+}}}{N^{Fe^{24+}}}\right)} \right) \tag{1.14}$$

The results of this analysis will be described in section 4.

1.3 R-Matrix Theory

In this study we use a non-perturbative method (the R-matrix approach) to calculate the electron-impact excitation data for each of the Fe-peak ions. As part of this we investigate the importance of including relativistic corrections in the calculations. This is done by performing both semi-relativistic calculations using the Intermediate-Coupling Frame-Transformation (ICFT) method [45] and fully relativistic calculations using the Dirac R-matrix suite of codes [46, 47]. Note that these methods include both direct excitation and resonant excitation. It has been shown previously [48] that radiation damping can be an important mechanism to include to get accurate low temperature rate coefficients. Thus, we also investigate this in our calculations.

Before describing the details of the methods used, it would be useful to consider first the process of electron-impact excitation in an atomic system, to illustrate the processes described above. Consider an excitation from the 1s^2 ($^1S_0$) level to the 1s2s ($^1S_0$) level. The atom is excited via a collision with a free electron, which loses the same amount of energy as the bound electrons gain. Thus, one can proceed via a direct excitation:

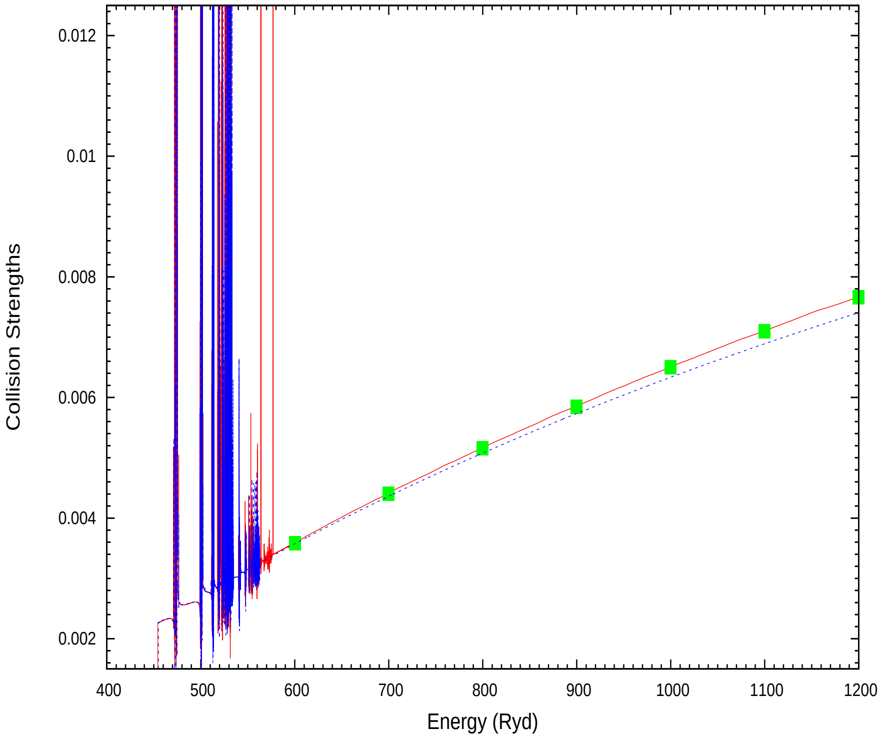

Figure 1.11: Example of a collision strength for Mn^{23+}. Note that the collision strength has a smooth part, corresponding to the direct excitation, and a part with resonant excitation features. The solid line (red) shows the results of our Dirac R-matrix calculations, the dashed line (blue) shows the results of our ICFT R-matrix calculations, and the squares shows the results from Aggarwal and Keenan [40].

$$1s^2(^1S_0) + e(\varepsilon_i) \rightarrow 1s2s(^1S_0) + e(\varepsilon_j) \tag{1.15}$$

where $\varepsilon_i - \varepsilon_j$ is equal to the difference between the 1s^2 $^1S_0$ and 1s2s $^1S_0$ levels. Note that this leads to the smooth background cross section seen in Figure 1.11. It is also possible to excite to the same level via a resonant excitation. This is a two step process, where first there is a dielectronic capture, e.g.

$$1s^2(^1S_0) + e(\varepsilon_i) \rightarrow 1s3snl \tag{1.16}$$

which is followed by an autoionization

$$1s3snl \rightarrow 1s2s(^1S_0) + e. \tag{1.17}$$

. This can only happen at the precise energy to capture into the 1s3snl configuration, leading to a sharp resonance in the excitation cross section at this energy. Note that there are a whole series of resonances for this 1s3snl process, and there are other possible core excitations (e.g. the 1s could be excited to the 3p, 3d, etc). This leads to a large number of resonance features in the collision cross section, see Figure 1.11.

For low charge states, due to the fact that autoionization rates are much larger than the radiative rates, the radiative rates can be ignored. However, for high charge states the two processes become competitive and one needs to account for possible radiative decay before the doubly excited state can autoionize. This is called ‘radiation damping’ and part of this work will be to determine whether it makes a significant change to the collision strengths for the He-like ions. Note that radiation damping would decrease the heights of the resonances in the collision strength, so the effect will be to decrease the net excitation.

The R-matrix calculations provide collision strengths for all transitions between the levels of the target ion. For modeling purposes, Maxwellian excitation rate coefficients are required, which can be expressed in terms of effective collision strengths. The effective collision strengths (Υ) are obtained by convolving the collision strengths (Ω) with a Maxwellian electron distribution.

$$\Upsilon_{ij} = \int_0^\infty \Omega_{ij} e^{\left(-\frac{E_j}{kT}\right)} d\left(\frac{E_j}{kT}\right) \tag{1.18}$$

where E_j is the energy of the outgoing electron and Ω_{ij} is the collision strength between levels i and j. The collision strength is proportional to the excitation cross section. These can be further transformed into collisional excitation ($q_{i\rightarrow j}$) and de-excitation ($q_{j\rightarrow i}$) rate coefficients.

$$\begin{aligned} q_{j\rightarrow i}(T_e) &= \frac{w_i}{w_j} e^{\frac{\Delta E_{ij}}{kT_e}} q_{i\rightarrow j}(T_e) \\ &= 2\sqrt{\pi}\alpha c a_o^2 \frac{1}{w_j} \left(\frac{I_H}{kT_e}\right)^{1/2} \Upsilon_{ij} \end{aligned} \quad (1.19)$$

where w is the statistical weight of the level and I_H is the Rydberg constant.

R-matrix theory was first introduced to describe nuclear reactions by Wigner and Eisenbud [49, 50]. It was later realized that the same method could be used to describe electron scattering. In R-matrix theory, configuration space is partitioned into 2 regions. For electron atom/ion collisions, a sphere of radius $r = a_0$ separates an internal region from an external region, r being the radial distance of the incident or scattered electron from the target nucleus, see Figure 1.12. The radius a_0 of the sphere is usually chosen so that it encompasses the charge distributions of the target eigenstates, or more simply, the radial extent of the most diffuse orbital in the target. In the internal region, where electron exchange and correlation effects between the scattered electron and the target electrons are important, a configuration interaction basis expansion of the total wave function is adopted.

The wavefunction representing the close-coupling expansion in the inner region is given by:

$$\Psi_k^{N+1} = A \sum_{i,j} a_{ijk} \psi_i^{N+1} \frac{u_{ij}(r_{N+1})}{r_{N+1}} + \sum_i b_{ik} \chi_i^{N+1} \ , \quad (1.20)$$

where A is an antisymmetrization operator, ψ_i^{N+1} are channel functions obtained by coupling N-electron target states with the angular and spin functions of the scattered electron, $u_{ij}(r)$ are radial continuum basis functions, and χ_i^{N+1} are bound functions which ensure completeness of the total wavefunction.

The resulting eigenvalues and eigenvectors are subsequently used in the formation of the R-matrix, which acts as the interface between the inner and outer region, is given by:

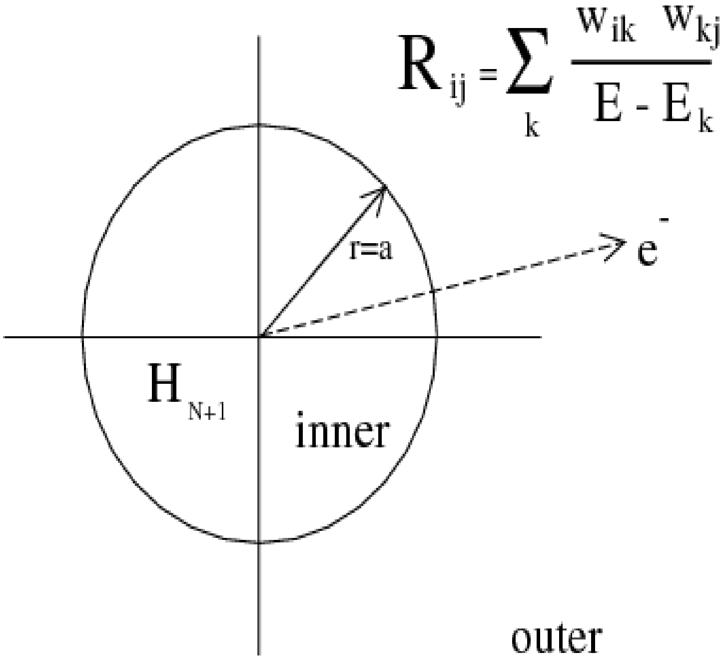

Figure 1.12: Overview of the R-matrix inner and outer region definitions

$$R_{ij}(E) = \frac{1}{2a_0} \sum_k \frac{w_{ik} w_{jk}}{E - E_k} \tag{1.21}$$

where E_k are the aforementioned eigenvalues of the $N+1$ electron Hamiltonian and w_{ik} are referred to as surface amplitudes. The w_{ik} are given by the following expression, where c_{ijk} correspond to the eigenvectors of the aforementioned Hamiltonian:

$$w_{ik} = \sum_j u_{ij} c_{ijk} \quad \text{at} \quad \mathrm{r} = \mathrm{a}_0 \tag{1.22}$$

1.3.1 Semi-Relativistic Intermediate Coupling Frame Transformation (ICFT) Method

The semi-relativistic Intermediate Coupling Frame Transformation method ([38]) was used to generate the collision strengths for each of the five He-like ion stages. One of the main benefits of the ICFT approach is that the majority of the calculation is carried out in an LS coupling scheme. The formation and diagonalization of the smaller LS resolved Hamiltonians (including mass-velocity and Darwin terms) is considerably less computationally demanding when compared to the formation and diagonalization of the corresponding jK or jJ level resolved Hamiltonians. Only in the final stages of the calculation, are the term-resolved K matrices transformed into level-to-level collision strengths. We note that when resolving hundreds of thousands of energy points, the generation of the LS resolved K-matrices is also more computationally efficient.

For all ions under consideration, the 1s-4f orbitals were generated from the atomic structure code, AUTOSTRUCTURE ([51]) and the resulting 29 LS terms were subsequently employed in our close-coupling expansion. The scattering calculation was performed with our set of parallel R-matrix programs ([52] and [53]), which are extensively modified versions of the serial RMATRIX I programs [54]). A basis of 70 continuum functions was used to span the energy range from the ground state to four times the ionization threshold for each of the helium-like systems under consideration.

For the collisional calculation, 50 partial waves ranging from $L = 0$ - 12 in total angular momentum were employed in the exchange calculation. A further 162 higher partial waves, ranging from $L = 13$ - 50, were also calculated, but neglecting exchange effects. The cross section results were then topped up for higher L using the method described by Burgess [55] for dipole transitions and a geometric series for non-dipole transitions. AUTOSTRUCTURE was also used to calculate infinite-energy Bethe/Born limit points using our semi-relativistic structure to allow us to interpolate our collision strengths to higher energies.

All of the R-matrix calculations implement the method of radiation damping as described in [48]. Meaningful radiative damping of resonance structure requires that the Rydberg sequences be resolved over the entire energy range.

Therefore, in the He-like Fe case, we systematically kept doubling the electron energy mesh in our cross sections until the differences in Maxwellian averaged rates from consecutive runs became negligible. As a consequence, a very fine energy mesh from the first to the last target threshold was adopted for use in each of the five cases under consideration, see section 4 for more details.

1.3.2 Dirac Atomic R-Matrix Code (DARC)

The target orbitals and energy levels for the present excitation calculations for the five He-like systems from Cr to Ni were generated using the Dirac-Hartree-Fock atomic structure program, GRASP0, within the Extended Average Level (EAL) approximation [46, 47]. The $1s^2$-$1s5g$ configurations gave rise to 49 levels, all of which were included within the close-coupling expansion of the subsequent scattering calculation. The size of the R-matrix 'box' is approximately 4.5 Bohr radii for all systems. We employed 70 basis orbitals for each continuum-electron angular momentum in order to comfortably span electron energies up to 4 Z^2 Ryd, where Z is the residual charge for each system. For partial wave J, ranging from 0.5 to 12.5, we used 120,000 energy points between the first excited $1s2s$ level and the final $1s5g$ level. Above the final threshold of the close-coupling expansion, a further 300 energy points were employed up to the 4 Z^2 Ryd limit. For higher partial waves, ranging from 13.5 to 39.5, 1000 pts were used from the first excitation threshold up to 4 Z^2 Ryd. The contribution from partial waves above 39.5 were estimated through the same procedure used for the ICFT calculations.

There are experimental energies for the majority but not all the levels in the points spectral data base [56]. Fortunately, these energy levels are complete for the n=2 and almost complete for the n=3 levels, which are the focus of the astrophysical modelling. Though our energy levels agree with the NIST values at the $< 1\%$ level, the $n = 2$ and $n = 3$ are shifted to NIST values for spectroscopic accuracy in the modeling.

The scattering calculations for electron-impact excitation were performed using our set of parallel Dirac R-matrix programs [57] which consist of significantly modified versions of the original DARC codes developed by Norrington et al. [58]. Also included were a set of modified programs from our suite of parallel Breit-Pauli R-matrix programs [54].

Due to the high-charge nature of the targets, we expect the radiative decay of the doubly excited resonant capture states to be competitive with the Auger rates. This has the effect of reducing the resonant excitation contribution to the effective collision strength. Thus, we require several bound-free dipole matrices to allow for radiation damping of Rydberg resonance sequences [48].

1.4 Thesis Objectives and Impact

It is clear that there is a wealth of spectral observations of Cr and Mn from SNR plasmas, but a lack of atomic data to take advantage of their diagnostic potential. In this thesis, we focus on the atomic data required for the He-like ion stages, which will be used, along with previous data for the H-like ion stages [24], to analyze the spectra of W49B.

In chapter 2, we investigate the atomic data required for spectroscopic accuracy, investigating relativistic effects and radiation damping of resonant excitation features. We compare with literature values where possible, and carry the new atomic data through to photon emissivities for use in spectral modeling. Chapter 3 then contains our spectral modeling results, based upon spectra of W49B. In that chapter, we determine whether recombination from the H-like ions is an important populating mechanism of the He-like emission lines. We then determine the fractional abundances of H-like and He-like Fe in W49B. This can be used to determine whether W49B is 'overionized'. Using these fractional abundances, we can then determine the elemental abundance of Cr and Mn (relative to Fe) in W49B. This can then be used to constrain the explosion mechanism for W49B.

Chapter 2

Atomic Data Results

2.1 Atomic Structure

Our final recommended data consist of our Dirac R-matrix results, based upon atomic relativistic orbital wavefunctions calculated using the GRASP [46, 47] atomic structure code. All levels in the $1s^2$ and $1snl$ ($2s \leq nl \leq 5g$) were included in the structure calculation. As an example of the accuracy of the atomic structure, we show the results for Cr and Mn in Tables 2.1 and 2.2. The results for the other ions are shown in Appendix A. We show a comparison with both NIST values and those recently calculated by Aggarwal and Keenan [40]. Our energies are within 0.1% of the NIST values and are in broad agreement with the results of Aggarwal and Keenan [40]. To ensure spectroscopic accuracy in our modeled emission features, we applied a small energy correction in order to match NIST values during the R-matrix calculation (before diagonalizing the Hamiltonian matrices). NIST energies were complete for the n=2 and 3 levels, but not for the n=4 and 5 levels. Therefore, we changed only the levels belonging to the n=2 and 3 configurations. Note that the energies given in Tables 2.1 and 2.2 are given solely to indicate the accuracy of the atomic structure calculations.

We show in Tables 2.3 and 2.4 a comparison of our A-values for the emission lines from the n=2 levels, which contribute to the Kα feature observed in the SNR plasmas. The A-values for the three non-dipole transitions are within 5% of the NIST values and the dipole rate is within 10% of the NIST value. Our final datafile contains all of the electric dipole, electric quadrupole, magnetic dipole, and magnetic quadrupole A-values between the levels in the file.

Table 2.1: Level energies from NIST compared to Aggarwal (2012) [40] and present energies for Cr^{22+}. Energies are in units of Rydbergs. Differences shown as percent differences between our results and those from NIST.

Configuration	Term	Level	NIST	Aggarwal	Present Work	Difference (%)
$1s^2$	^1S	0	0.00000	0.00000	0.00000	0.0000
$1s2s$	^3S	1	413.57044	413.89676	413.90944	0.0819
$1s2p$	^3P	0	415.50050	415.73834	415.74971	0.0599
$1s2p$	^3P	1	415.62307	415.95718	415.96860	0.0831
$1s2s$	^1S	0	415.66909	415.97150	415.98222	0.0753
$1s2p$	^3P	2	416.37450	416.72891	416.73996	0.0877
$1s2p$	^1P	1	417.62303	417.99628	418.00903	0.0923
$1s3s$	^3S	1	489.89810	490.24042	490.25290	0.0724
$1s3p$	^3P	0	490.43035	490.74927	490.76148	0.0675
$1s3s$	^1S	0	490.45477	490.79056	490.80249	0.0708
$1s3p$	^3P	1	490.46589	490.81137	490.82361	0.0729
$1s3p$	^3P	2	490.69033	491.04138	491.05349	0.0740
$1s3d$	^3D	2	490.98194	491.32523	491.33762	0.0724
$1s3d$	^3D	1	490.97829	491.33188	491.34430	0.0745
$1s3p$	^1P	1	491.02768	491.38391	491.39635	0.0750
$1s3d$	^3D	3	491.06540	491.41779	491.43020	0.0742
$1s3d$	^1D	2	491.08327	491.43011	491.44255	0.0731
$1s4s$	^3S	1	516.31020	516.66315	516.67560	0.0707
$1s4p$	^3P	0	516.53400	516.87256	516.88493	0.0679
$1s4s$	^1S	0	516.54350	516.88733	516.89958	0.0689
$1s4p$	^3P	1	516.54900	516.89838	516.91075	0.0700
$1s4p$	^3P	2	516.64380	516.99548	517.00780	0.0704
$1s4d$	^3D	2	516.76680	517.11182	517.12426	0.0691
$1s4d$	^3D	1	516.76500	517.11530	517.12774	0.0701
$1s4p$	^1P	1	516.78590	517.13593	517.14833	0.0701
$1s4d$	^3D	3	516.80140	517.15094	517.16336	0.0700
$1s4d$	^1D	2	516.80870	517.15771	517.17015	0.0699
$1s4f$	^3F	2		517.15784	517.17031	N/A
$1s4f$	^3F	3		517.15790	517.17037	N/A
$1s4f$	^3F	4		517.17731	517.18976	N/A
$1s4f$	^1F	3		517.17737	517.18984	N/A

n=5 level energies for Cr, continued from previous page

Configuration	Term	Level	NIST	Aggarwal	Present Work	Difference (%)
$1s5s$	^3S	1	528.46840	528.82111	528.83357	0.0691
$1s5p$	^3P	0	528.57900	528.92706	528.93944	0.0681
$1s5s$	^1S	0	528.58770	528.93475	528.94708	0.0679
$1s5p$	^3P	1	528.59050	528.94019	528.95259	0.0685
$1s5p$	^3P	2	528.63880	528.98987	529.00224	0.0687
$1s5d$	^3D	1		529.04858	529.06104	N/A
$1s5d$	^3D	2		529.05054	529.06295	N/A
$1s5p$	^1P	1	528.71170	529.06116	529.07359	0.0684
$1s5d$	^3D	3		529.06860	529.08106	N/A
$1s5d$	^1D	2		529.07245	529.08489	N/A
$1s5f$	^3F	2		529.07251	529.08495	N/A
$1s5f$	^3F	3		529.07257	529.08500	N/A
$1s5f$	^3F	4		529.08246	529.09491	N/A
$1s5f$	^1F	3		529.08252	529.09498	N/A
$1s5g$	^3G	3		529.08252	529.09499	N/A
$1s5g$	^3G	4		529.08252	529.09499	N/A
$1s5g$	^3G	5		529.08850	529.10095	N/A
$1s5g$	^1G	4		529.08850	529.10095	N/A

Table 2.2: Level energies from NIST compared to Aggarwal (2012) [40] and present energies for Mn^{23+}. Energies are in units of Rydbergs. Differences shown are percent differences between our results and those from NIST.

Configuration	Term	Level	NIST	Aggarwal	Present Work	Difference (%)
$1s^2$	^1S	0	0.00000	0.00000	0.00000	0.0000
$1s2s$	^3S	1	449.89473	450.29355	450.30678	0.0915
$1s2p$	^3P	0	451.92280	452.22052	452.23253	0.0685
$1s2p$	^3P	1	452.09817	452.46436	452.47566	0.0834
$1s2s$	^1S	0	452.05860	452.46750	452.47958	0.0930
$1s2p$	^3P	2	452.96470	453.39484	453.40647	0.0974
$1s2p$	^1P	1	454.25405	454.70160	454.71493	0.1014
$1s3s$	^3S	1	532.98920	533.40778	533.42082	0.0809
$1s3p$	^3P	0	533.54870	533.94031	533.95313	0.0757
$1s3s$	^1S	0	533.57400	533.98303	533.99558	0.0789
$1s3p$	^3P	1	533.58790	534.01019	534.02300	0.0815
$1s3p$	^3P	2	533.85850	534.28674	534.29940	0.0825
$1s3d$	^3D	2	534.16380	534.58356	534.59655	0.0809
$1s3d$	^3D	1	534.15920	534.59064	534.60365	0.0831
$1s3p$	^1P	1	534.20750	534.63971	534.65271	0.0833
$1s3d$	^3D	3	534.26310	534.69336	534.70635	0.0829
$1s3d$	^1D	2	534.28230	534.70618	534.71919	0.0817
$1s4s$	^3S	1	561.74780	562.18073	562.19377	0.0793
$1s4p$	^3P	0	561.98390	562.39990	562.41287	0.0763
$1s4s$	^1S	0	561.99480	562.41510	562.42792	0.0770
$1s4p$	^3P	1	562.00120	562.42889	562.44188	0.0784
$1s4p$	^3P	2	562.11500	562.54565	562.55858	0.0788
$1s4d$	^3D	1	562.24080	562.66736	562.68039	0.0781
$1s4d$	^3D	2	562.24300	562.67108	562.68410	0.0784
$1s4p$	^1P	1	562.26270	562.69031	562.70335	0.0783
$1s4d$	^3D	3	562.28280	562.71375	562.72675	0.0789
$1s4d$	^1D	2	562.29460	562.72076	562.73380	0.0780
$1s4f$	^3F	2		562.72101	562.73405	N/A
$1s4f$	^3F	3		562.72107	562.73411	N/A
$1s4f$	^3F	4		562.74408	562.75711	N/A
$1s4f$	^1F	3		562.74414	562.75719	N/A

n=5 level energies for Mn, continued from previous page

Configuration	Term	Level	NIST	Aggarwal	Present Work	Difference (%)
$1s5s$	^3S	1	574.99040	575.42078	575.43384	0.0771
$1s5p$	^3P	0	575.10750	575.53168	575.54465	0.0760
$1s5s$	^1S	0	575.11520	575.53949	575.55244	0.0760
$1s5p$	^3P	1	575.11790	575.54639	575.55940	0.0767
$1s5p$	^3P	2	575.17630	575.60614	575.61911	0.0769
$1s5d$	^3D	1		575.66760	575.68061	N/A
$1s5d$	^3D	2		575.66962	575.68266	N/A
$1s5p$	^1P	1	575.25190	575.67957	575.69258	0.0765
$1s5d$	^3D	3		575.69135	575.70435	N/A
$1s5d$	^1D	2		575.69531	575.70833	N/A
$1s5f$	^3F	2		575.69543	575.70844	N/A
$1s5f$	^3F	3		575.69543	575.70849	N/A
$1s5f$	^3F	4		575.70721	575.72025	N/A
$1s5f$	^1F	3		575.70728	575.72032	N/A
$1s5g$	^3G	3		575.70728	575.72033	N/A
$1s5g$	^3G	4		575.70728	575.72033	N/A
$1s5g$	^3G	5		575.71436	575.72741	N/A
$1s5g$	^1G	4		575.71436	575.72741	N/A

Table 2.3: Table of radiative rates (A_{ji} in s^{-1}) for Cr XXIII transitions from the ground to the n=2 shell.

Transition	Present Work	Aggarwal (2012)	NIST
1s2s(^{3}S$_1$) → 1s^2 (^{1}S$_0$)	8.900×10^{7}	8.876×10^{7}	9.370×10^{7}
1s2p(^{3}P$_1$) → 1s^2 (^{1}S$_0$)	2.050×10^{13}	2.339×10^{13}	2.340×10^{13}
1s2p(^{3}P$_2$) → 1s^2 (^{1}S$_0$)	3.350×10^{9}	3.363×10^{9}	3.450×10^{9}
1s2p(^{1}P$_1$) → 1s^2 (^{1}S$_0$)	3.470×10^{14}	3.437×10^{14}	3.370×10^{14}

Table 2.4: Table of radiative rates (A_{ji} in s^{-1}) for Mn XXIV transitions from the ground to the n=2 shell.

Transition	Present Work	Aggarwal (2012)	NIST
1s2s(^{3}S$_1$) → 1s^2 (^{1}S$_0$)	1.3500×10^{8}	1.3500×10^{8}	1.4200×10^{8}
1s2p(^{3}P$_1$) → 1s^2 (^{1}S$_0$)	2.8700×10^{13}	3.259×10^{13}	3.2500×10^{13}
1s2p(^{3}P$_2$) → 1s^2 (^{1}S$_0$)	4.7300×10^{9}	4.704×10^{9}	4.8200×10^{9}
1s2p(^{1}P$_1$) → 1s^2 (^{1}S$_0$)	4.0600×10^{14}	4.016×10^{14}	3.9300×10^{14}

It has been previously shown [59] that the two-photon transition between the 1s^2 (^{1}S$_0$) and 1s2s(^{1}S$_0$) levels is important to include in the population modeling of He-like systems. Without this A-value, the only decay route possible for the 1s2s(^{1}S$_0$) level is a very weak transition to the 1s2s(^{3}S$_1$) level. This leads to a significantly increased population in the 1s2s(^{3}S$_1$) level and an overestimation of the 1s2s(^{3}S$_1$) → 1s^2 (^{1}S$_0$) spectral line. Thus, the two-photon transition, while not contributing a spectral line to the Kα emission feature, is important for the population modeling. The GRASP calculation does not evaluate spontaneous emission coefficient for $j \rightarrow k$ ($A_{j \rightarrow k}$) for two-photon transitions, so we supplemented each of our datasets with a two-photon A-value from the literature. We used the two-photon A-values of Derevianko and Johnson [60]. In their publication, Derevianko and Johnson report on their relativistic calculations for two-photon decay rates of He-like ions with nuclear charges in the range Z = 2-100. Thus, we performed an interpolation of their data to determine A-values for the five ions used in this thesis. Table 2.5 shows these decay rates.

Table 2.5: Table of two-photon A-values used for the He-like Fe-peak element ions, obtained by interpolation of the data of Derevianko and Johnson [60].

Ion	A$_{1s2s(^1S_0)\rightarrow 1s^2(^1S_0)}$
Cr^{22+}	2.526×10^9
Mn^{23+}	3.249×10^9
Fe^{24+}	4.135×10^9
Co^{25+}	5.214×10^9
Ni^{26+}	6.517×10^9

2.2 Collision Strengths

The orbital wave functions obtained as part of the GRASP structure calculations were used in our Dirac *R*-matrix calculations to obtain electron-impact collision strengths transitions between all levels in the calculation. The details of the calculation are already given in Section 2.3. The DARC calculations resulted in 1176 transitions between the 49 levels.

We performed Dirac *R*-matrix calculations for each of the ions, in each case with and without the effects of radiation damping included. To determine the contribution that the fully relativistic approach has, compared to a semi-relativistic approach, we also calculated ICFT *R*-matrix collision strengths (with and without radiation damping).

We compare first our collision strengths for Cr, see Figures 2.1 and 2.2. Figure 2.1 shows a comparison of our collision strength data for four of the transitions from the ground to the n=2 shell. In each case, our results are in close agreement with those of Aggarwal and Keenan [40] and the background collision strengths are within 5% of the semi-relativistic ICFT data. Considering the $1s^2$ $(^1S_0) \rightarrow 1s2s(^1S_0)$ collision strength (Figure 2.2), one sees much more significant differences between the DARC and ICFT results, with the DARC results being about 15% higher than the ICFT data. To determine if the differences are due to relativistic effects in the structure or in the scattering calculations, our colleagues calculated Relativistic Convergent Close Coupling (RCCC) collision strengths for Cr (Bray, I., private communication). The RCCC results are in good agreement with the DARC collision strengths. A CCC calculation using the same relativistic structure, but with a semi-relativistic scattering calculation was then performed, finding very little difference in the final collision strength. This indicates that it is relativistic effects of the target orbital wave functions, rather than the scattering, that causes the increase in the collision strength. Note that while the figures shown are for Cr^{22+}, the other ions show very similar results. Figures for the other ions are shown in Appendix B.

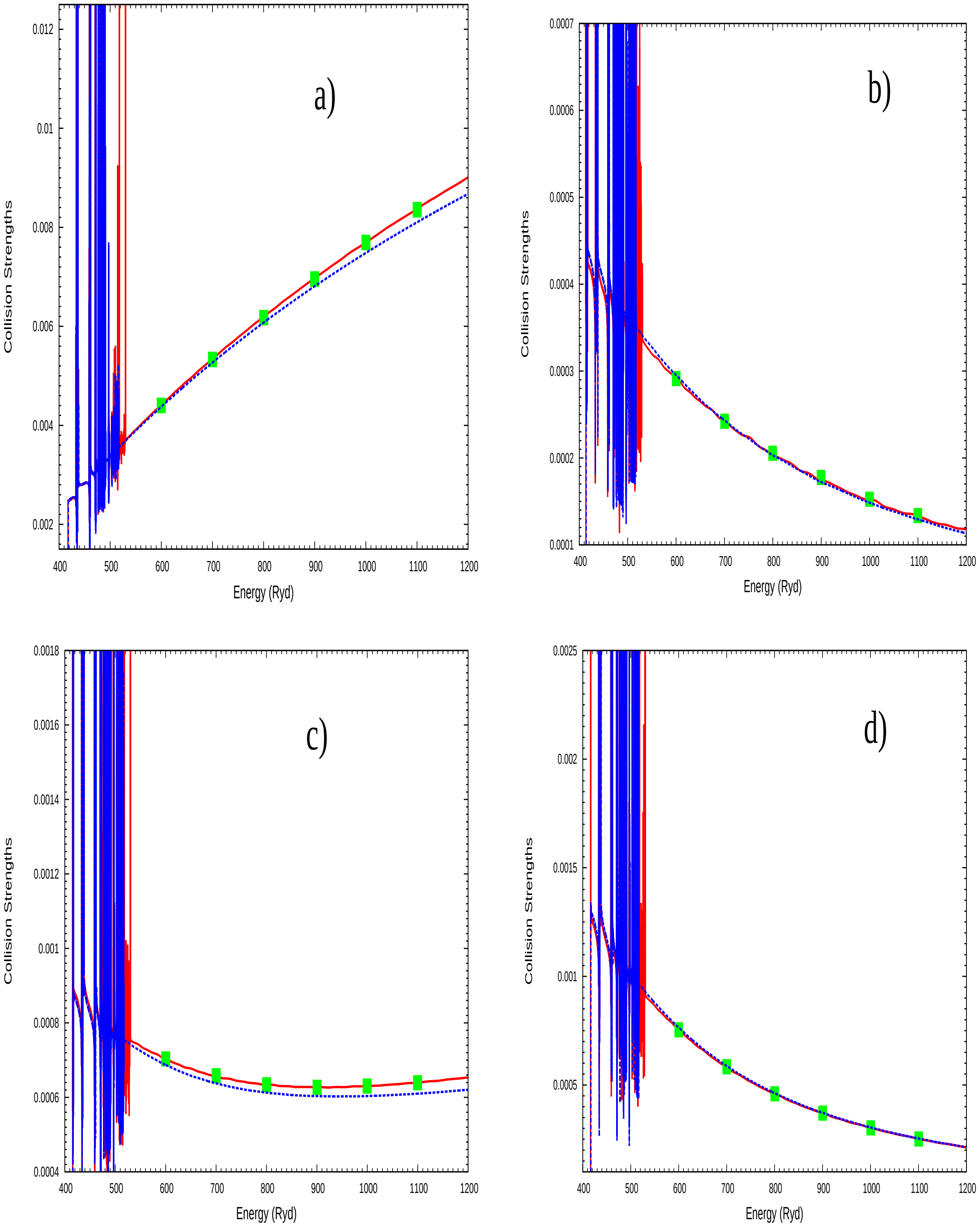

Figure 2.1: Collision strength for the a)$1s^2$ ($^1S_0$) → $1s2p(^1P_1)$ b)$1s^2$ ($^1S_0$) → $1s2s(^3S_1)$ c)$1s^2$ ($^1S_0$) → $1s2p(^3P_1)$ d)$1s^2$ ($^1S_0$) → $1s2p(^3P_2)$ transitions for Cr^{22+}. The solid line (red) shows the DARC damped calculation, the dashed line (blue) shows the ICFT damped calculation, and the results of Aggarwal and Keenan [40] are shown by solid squares.

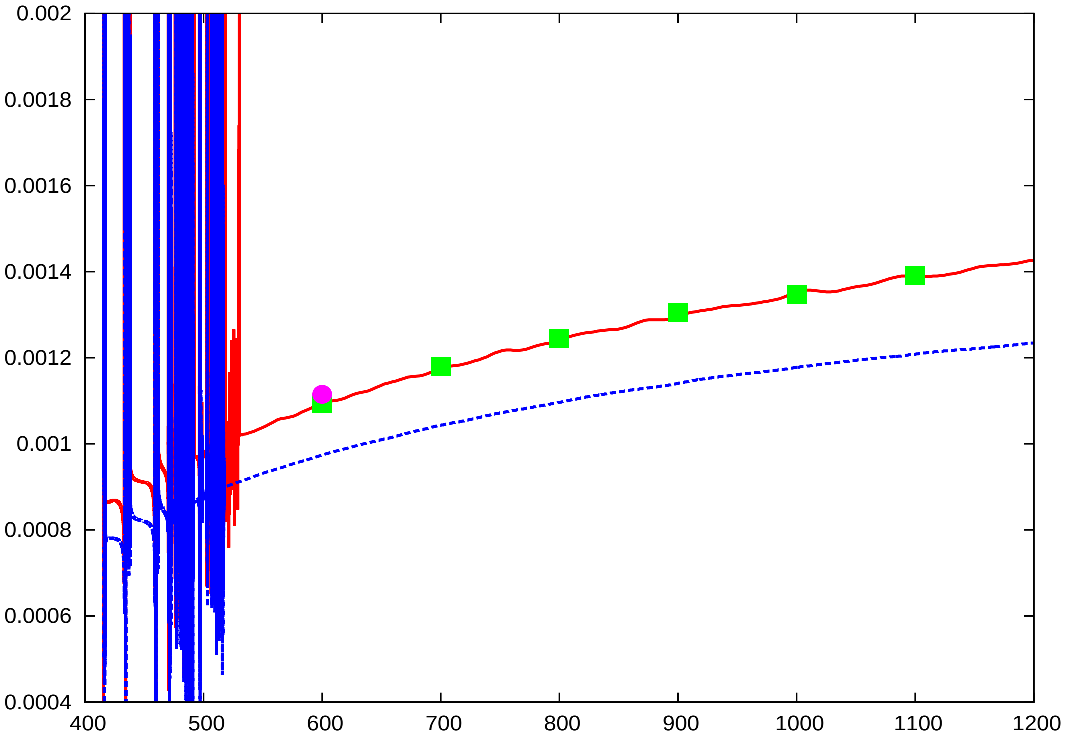

Figure 2.2: Collision strength for the 1s^2 (^{1}S$_0$) → 1s2s (^{1}S$_0$) transition for Cr^{22+}. The solid line (red) shows the DARC damped calculation and the dashed line (blue) shows the ICFT damped calculation. The results of Aggarwal and Keenan [40] are shown by solid squares. Also shown are the RCCC results (solid circle).

2.3 Effective Collision Strengths

Our collision strengths were supplemented with infinite-energy Bethe/Born limit to allow the collision strengths to be extrapolated to higher energies. The collision strengths were then converted into effective collision strengths using Equation 1.18. As part of this process, we investigated the convergence of the effective collision strengths with energy mesh resolution. Taking Ni^{26+}, being the ion with the narrowest resonances and thus the most difficult to resolve, we performed a series of outer region calculations with progressively finer energy meshes. We compared the effective collision strengths of a 120,000 mesh point run with those of 240,000 and 480,000 energy points in the resonance region. We found that the 120,000 mesh point run was sufficient to converge the effective collision strengths at the lowest temperature. 98.8% of the transitions are converged to within 2% of each other, and 99.9% are converged to within 4% of each other. For excitations from ground level, 97.9% are converged to within 1% and all of the transitions from the ground are converged to within 2%. Thus, we used 120,000 energy mesh points in all of our calculations of the resonance region for each of our ions. We also used a fine mesh in the final ICFT calculations. Figure 2.3 shows a scatter plot of the ratio of the effective collision strengths between the 120,000 and 240,000 mesh point files, for a temperature of 1×10^6 K.

We then investigated the role of radiation damping on the effective collision strengths. Figures 2.4 and 2.5 show the results for transitions to the n=2 shell from the ground. For the dipole transition (Figure 2.4a) all of the methods agree with each other, as one would expect for a transition where the resonance contribution is negligible. In general, radiation damping can decrease the effective collision strengths by about 10% at the lowest temperatures, with the differences becoming negligible by 1×10^7K. We note that the differences in the background collision strengths from Figures 2.1 and 2.2 are also observed in the effective collision strengths. For example, $1s^2$ $(^1S_0) \rightarrow 1s2s(^1S_0)$ transition (Figure 2.5) shows a 15% increase in the DARC results compared with the ICFT data, due to the similar change in the background collision strength (Figure 2.2). Our results are in broad agreement with those

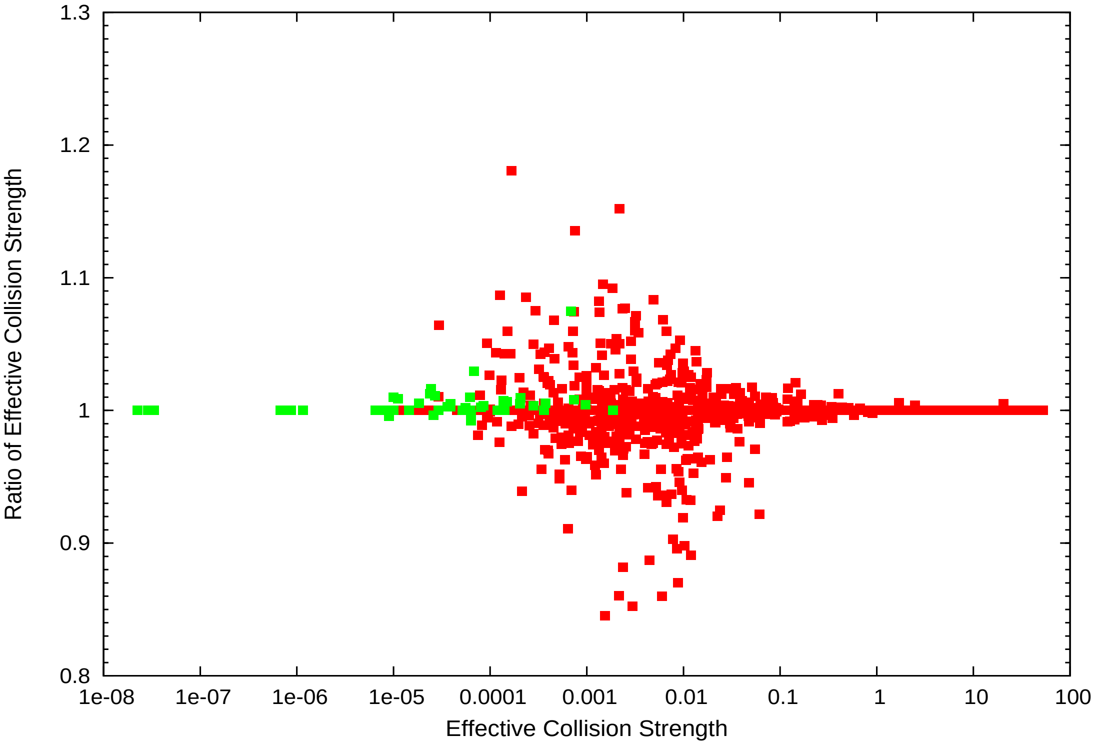

Figure 2.3: Ratio of effective collision strengths for He-like Ni for Te= 1×10^6. The ratio compares the 120k and 240k files. The green squares shows just the transitions from the ground, while the red squares shows all of the transitions in the file.

of Aggarwal and Keenan [40], with the differences largely being at the lowest temperatures. The differences are most likely due to a combination of resonance resolution and the effects of radiation damping, which was not included in their calculation. Again, while the figures show the comparison for Cr^{22+}, the other ions show very similar results. Appendix C shows the figures for the other ions.

Our final recommended data consist of Maxwellian effective collision strengths generated from the DARC damped calculations for each of the ions.

2.4 Photon Emissivity Coefficients (PEC)

Our final recommended atomic data consist of our DARC damped effective collision strengths, the set of A-values from our GRASP calculation (supplemented with the two-photon A-value), and recombination rate coefficients taken from the literature. The radiative recombination rate coefficients were calculated using a Gaunt factor approach [25], which for a hydrogenic system recombining to a He-like one gives results within a few percent of the distorted-wave calculations of Badnell [51]. While radiative recombination dominates the recombination at low temperatures, by 2 keV DR makes a similar size contribution and so should be accounted for. The dielectronic recombination rate coefficients were taken from the level-resolved distorted-wave calculations of Badnell [51]. For each of the ions under consideration, this allowed the generation of both excitation and recombination photon emissivity coefficients.

Before describing the abundance diagnostics that we performed for the SNR spectra, we first consider the contributions to the total Kα photon emissivity and the effects of data quality of the total PEC. Figure 2.6 shows the total Kα PEC for Fe as a function of electron temperature. Note that the dipole transition contributes about half of the total emission in the temperature range of interest for W49B SNR. Thus, the effects described previously (radiation damping and relativistic effects) could affect the total Kα PEC. We find that the ICFT damped Kα PEC is about 5% lower than the DARC PEC values. If one considers

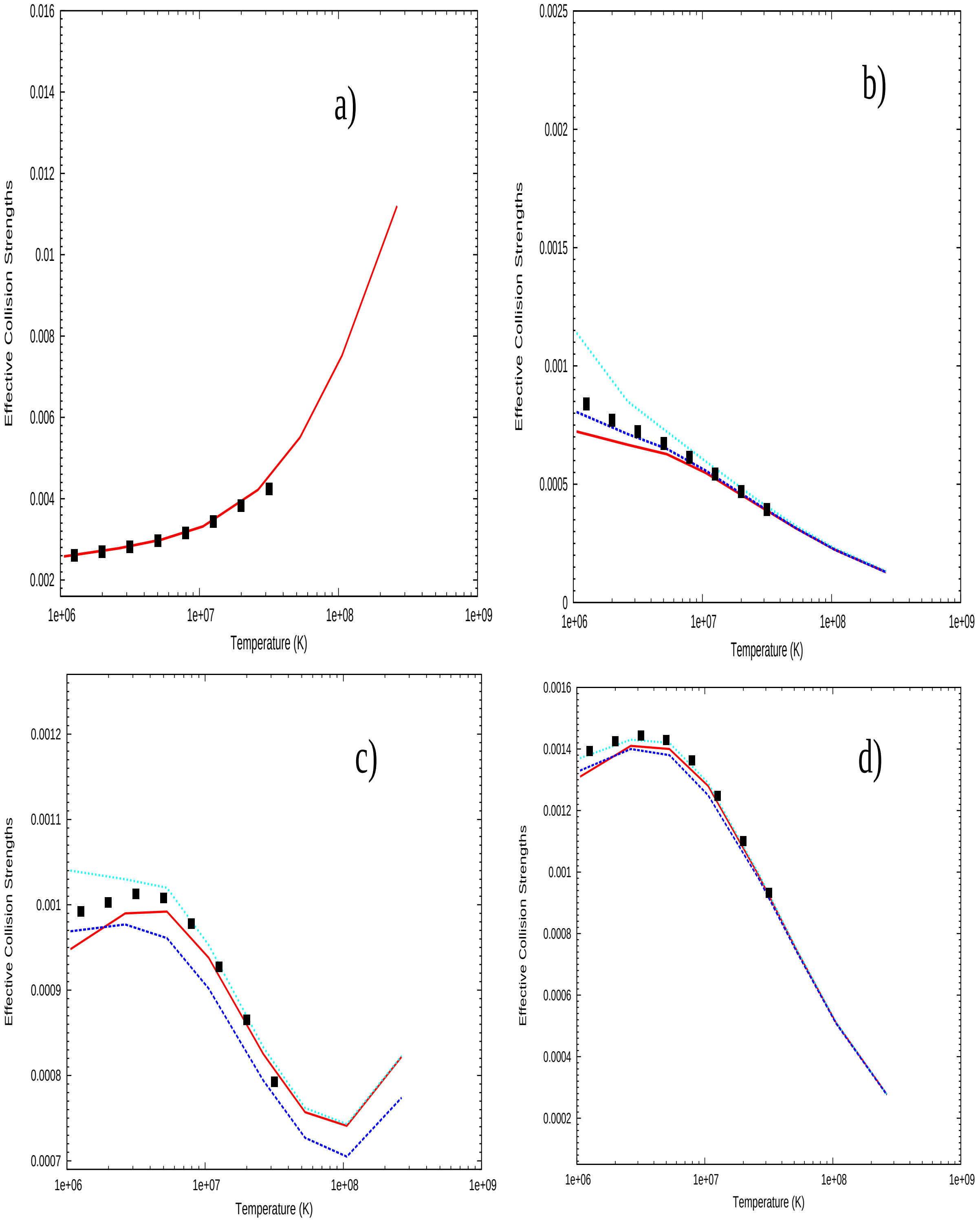

Figure 2.4: Effective collision strength for the a) $1s^2(^1S_0) \rightarrow 1s2p(^1P_1)$ b) $1s^2(^1S_0) \rightarrow 1s2s(^3S_1)$ c) $1s^2(^1S_0) \rightarrow 1s2p(^3P_1)$ d) $1s^2(^1S_0) \rightarrow 1s2p(^3P_2)$ transitions for Cr^{22+}. The solid line (red) shows the DARC damped calculation, the light blue line shows the DARC undamped calculation and the dark blue line shows the ICFT damped calculation. The results of Aggarwal and Keenan [40] are shown by solid squares. Note that in figure a) the calculations all give very similar results and cannot be resolved on the plot.

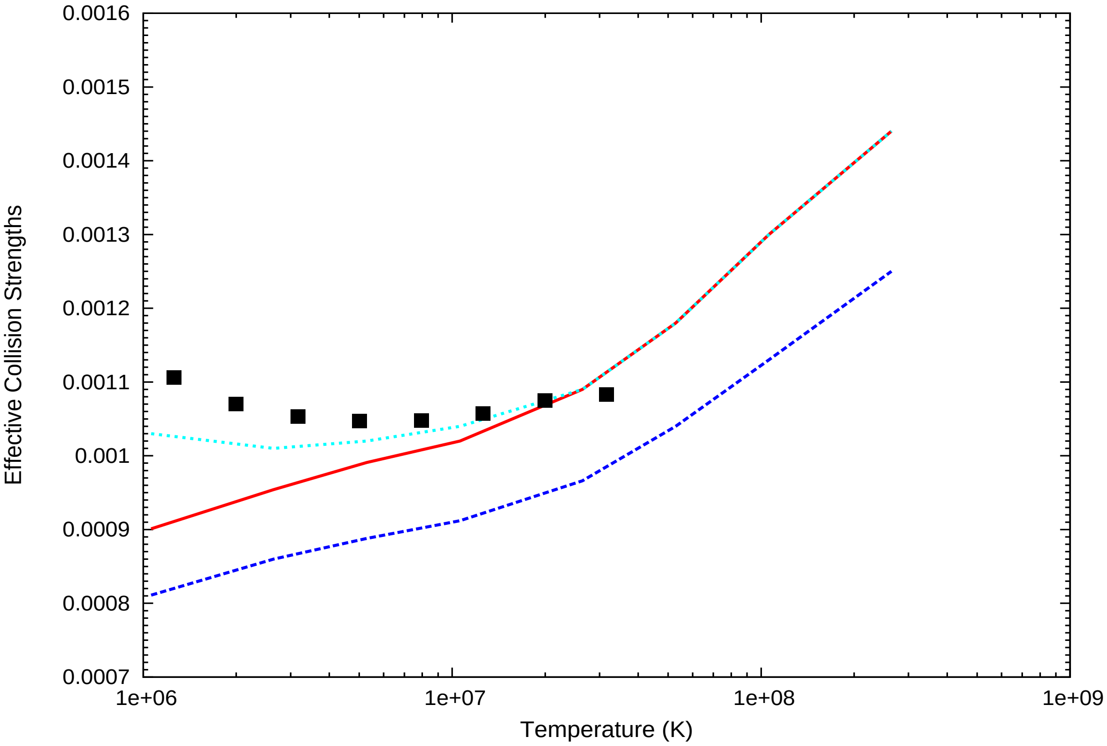

Figure 2.5: Effective collision strength for the $1s^2(^1S_0) \rightarrow 1s2s\ (^1S_0)$ transition for Cr^{22+}. The solid line (red) shows the DARC damped calculation and the dashed line (light blue) shows the DARC undamped calculations. The ICFT damped calculations are shown by the dark blue line. The results of Aggarwal and Keenan [40] are shown by solid squares.

only the x+y+z PEC, the difference is about 8%, see Figure 2.7. Radiation damping reduces the Kα PEC by about 3%. If one considers the effect of damping on the PEC for the x+y+z PEC, the difference is about 5%, see Figure 2.7. Thus, while the effects investigated in section 3.2 and 3.3 do not make a significant difference to the total Kα PEC, they should be included when looking at individual line intensities. Figure 2.8 shows the trends in the total Kα PEC^{ex} along the iso-electronic sequence. The smooth trend suggests that one could extrapolate our data to other nearby members of the iso-electronic sequence.

As mentioned previously, the two photon transition is important for the population modeling of these ions. Figure 2.9 shows the ratio of the Fe Kα PEC with the two-photon rate included in the modeling, to the PEC when this A-value is omitted. Note that the two-photon transition is not included as a line in the Kα emissivity, only in the population modeling. Thus, the two-photon transition is causing a difference in one of the Kα transition. The effect of omitting the two photon A-value is to increase the population in the 1s2s ^{3}S$_1$ level. This level can be populated from the upper level of the two-photon decay, but the rate is so small as to not affect the modeling (because the two photon-decay causes most of the electrons in the 1s2s $^1S_0$ level to decay to the ground). However, if this two-photon value is omitted, then a huge amount of population builds up in the 1s2s^{1}S$_0$ level, which then increases the population of the 1s2s^{3}S$_1$ level. Thus, if one does not include the A-value in the collisional-radiative modeling one gets PEC values for the Z-line that are artificially high. Note that the size of this effect is larger than the effect of relativistic corrections or radiation damping on the final Kα PEC.

Figure 2.10 shows the total Kα PEC^{ex} and PEC^{rec} coefficients as a function of electron temperature for Fe^{24+}. Note that when evaluating the total emissivity for Fe Kα one would multiply the PEC^{ex} by the fractional population in the He-like ion stage and the PEC^{rec} by the fractional population in the H-like ion stage. Thus, this plot gives an indication of what the relative abundances would have to be for the H-like ion stage to be a significant

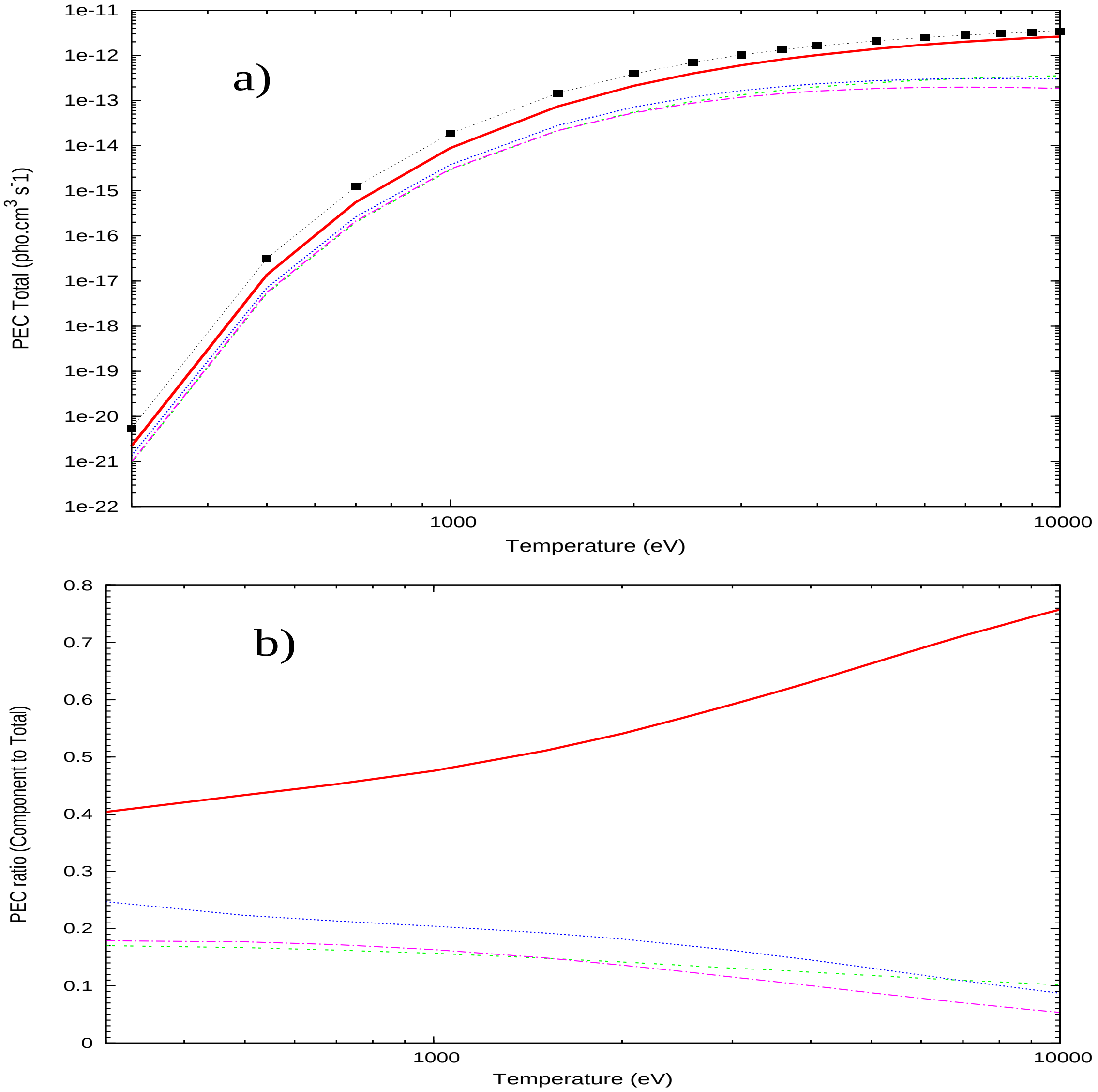

Figure 2.6: Components of the total Kα emission for Fe^{24+}. In a) the dashed line with squares shows the total Kα PEC. The solid line shows the total PEC for the W line, the dotted line shows the total for the x line, the dot-dashed line shows the total for the y line, and the double dot-dashed line shows the PEC for the z line.

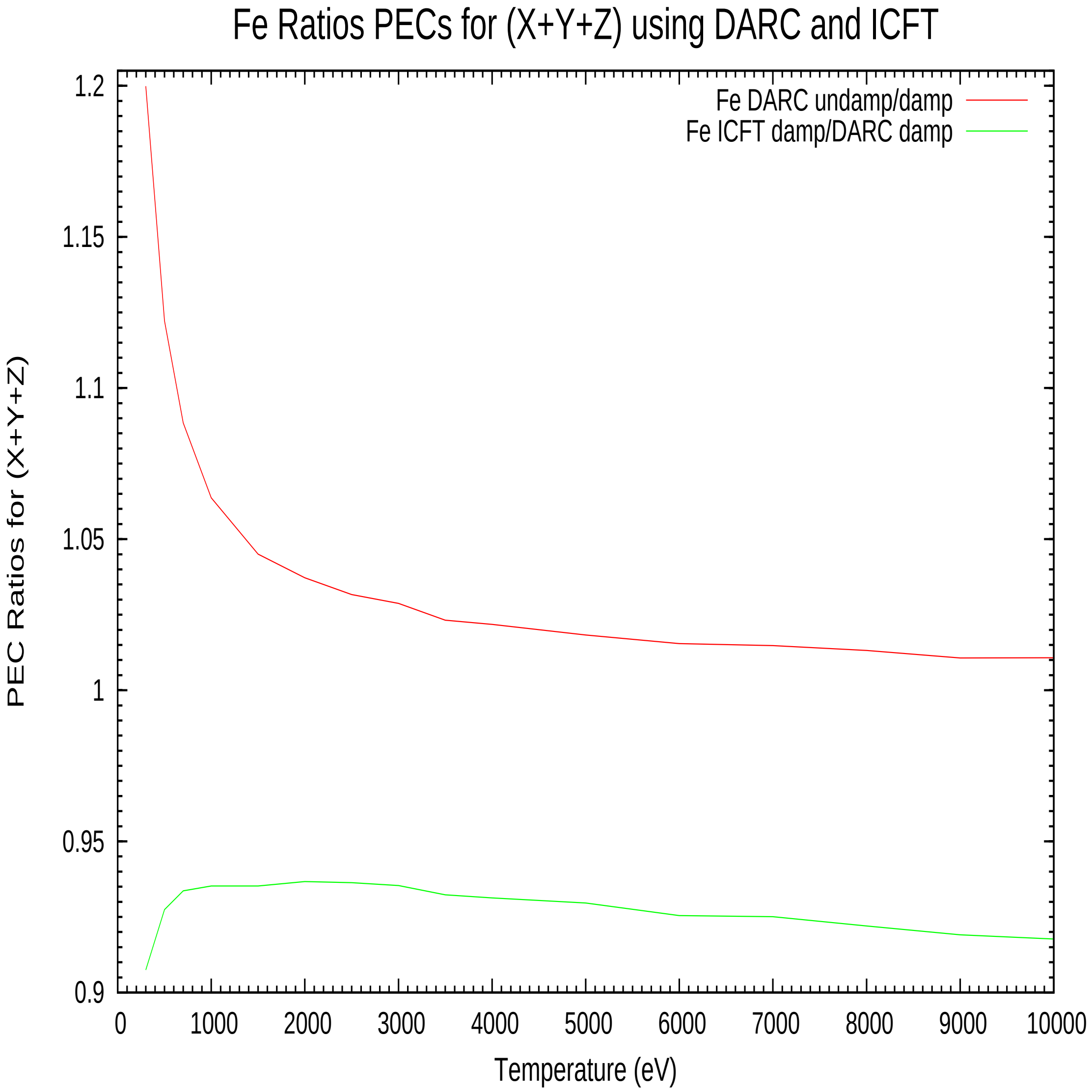

Figure 2.7: Ratio of the DARC to ICFT Kα PEC^{ex} (green line), and the ratio of the DARC damped to undamped Kα PEC^{ex} (red line) to show the effects of the fully relativistic method and radiation damping.

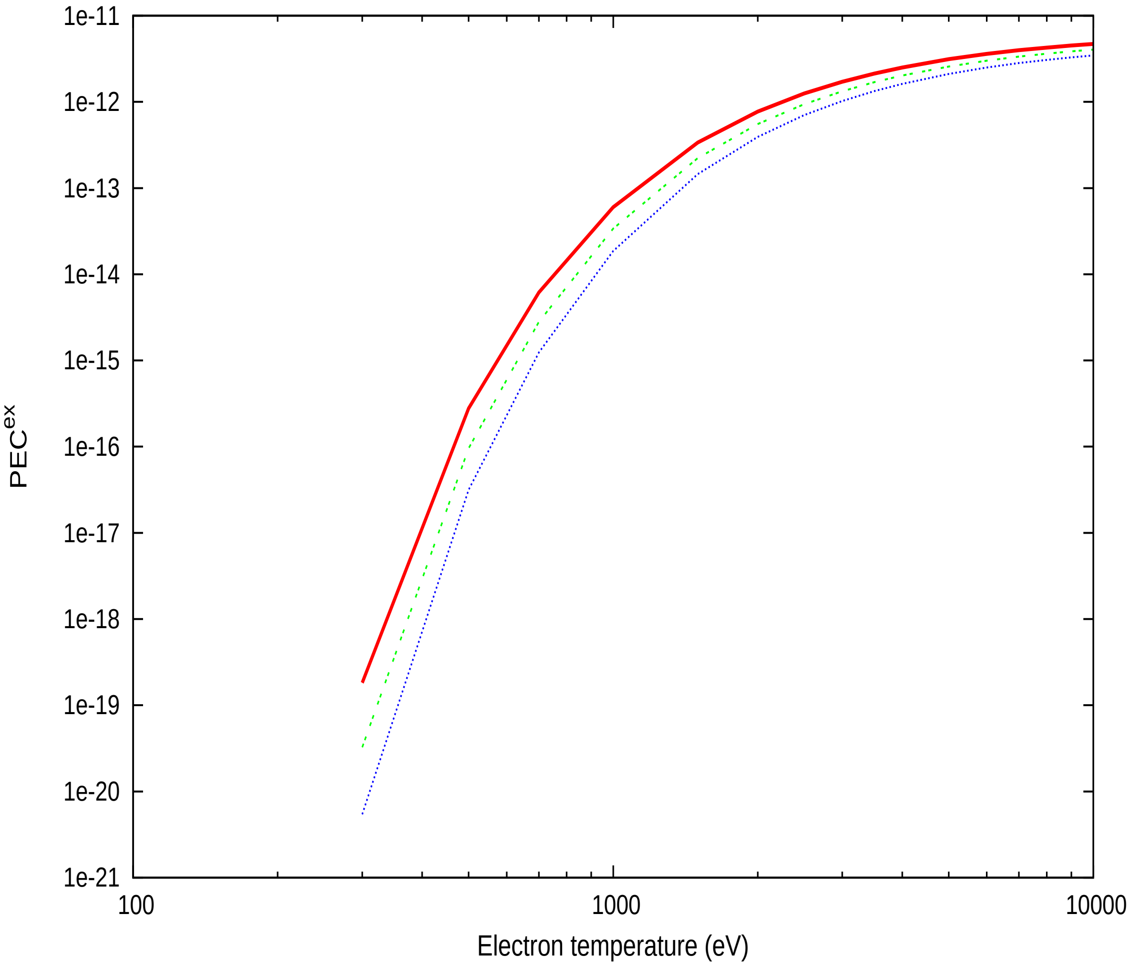

Figure 2.8: Kα PEC^{ex}, for Cr, Mn, and Fe as a function of electron temperature. The solid line shows the results for Cr, the dashed line shows the results for Mn and the dotted line shows the results for Mn.

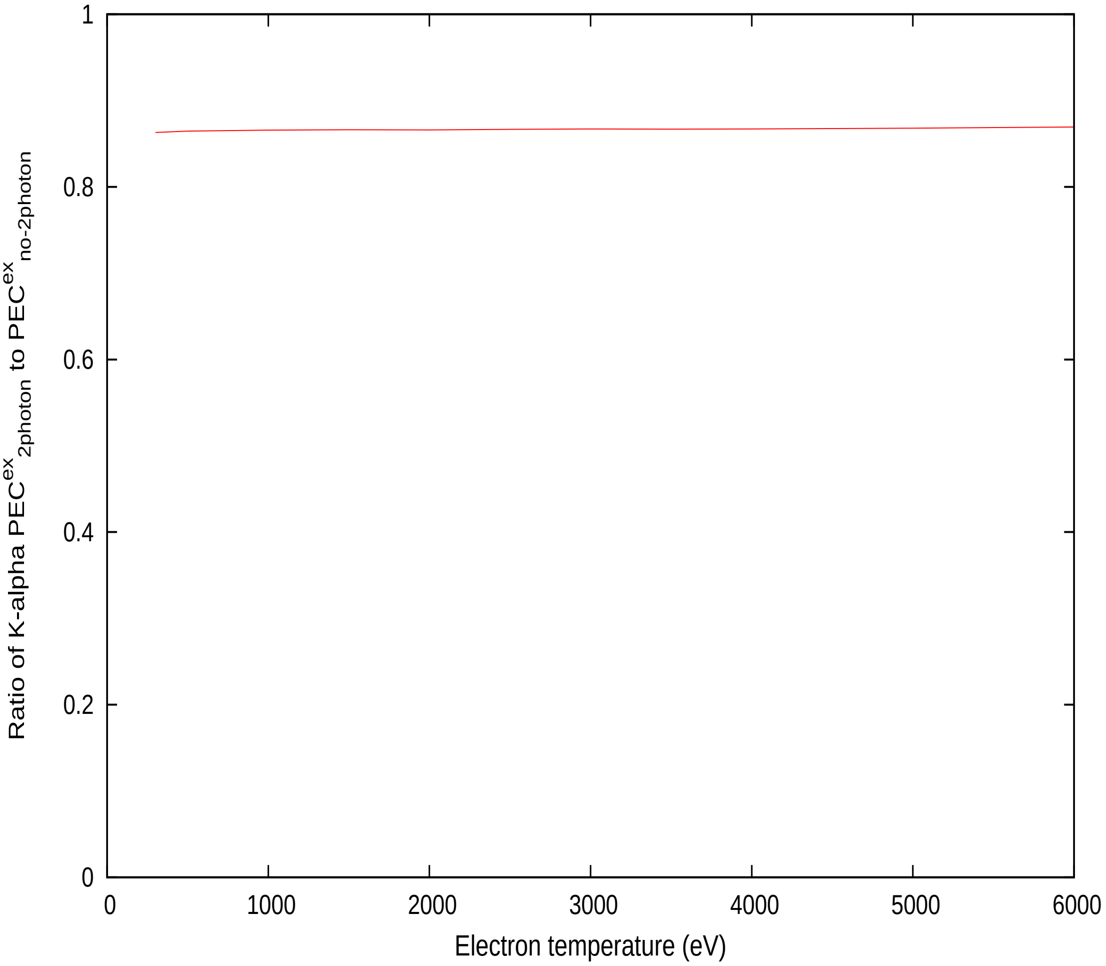

Figure 2.9: Ratio of Fe Kα PEC^{ex} with the two-photon A-value included to the Fe Kα PEC^{ex} without the A-value included.

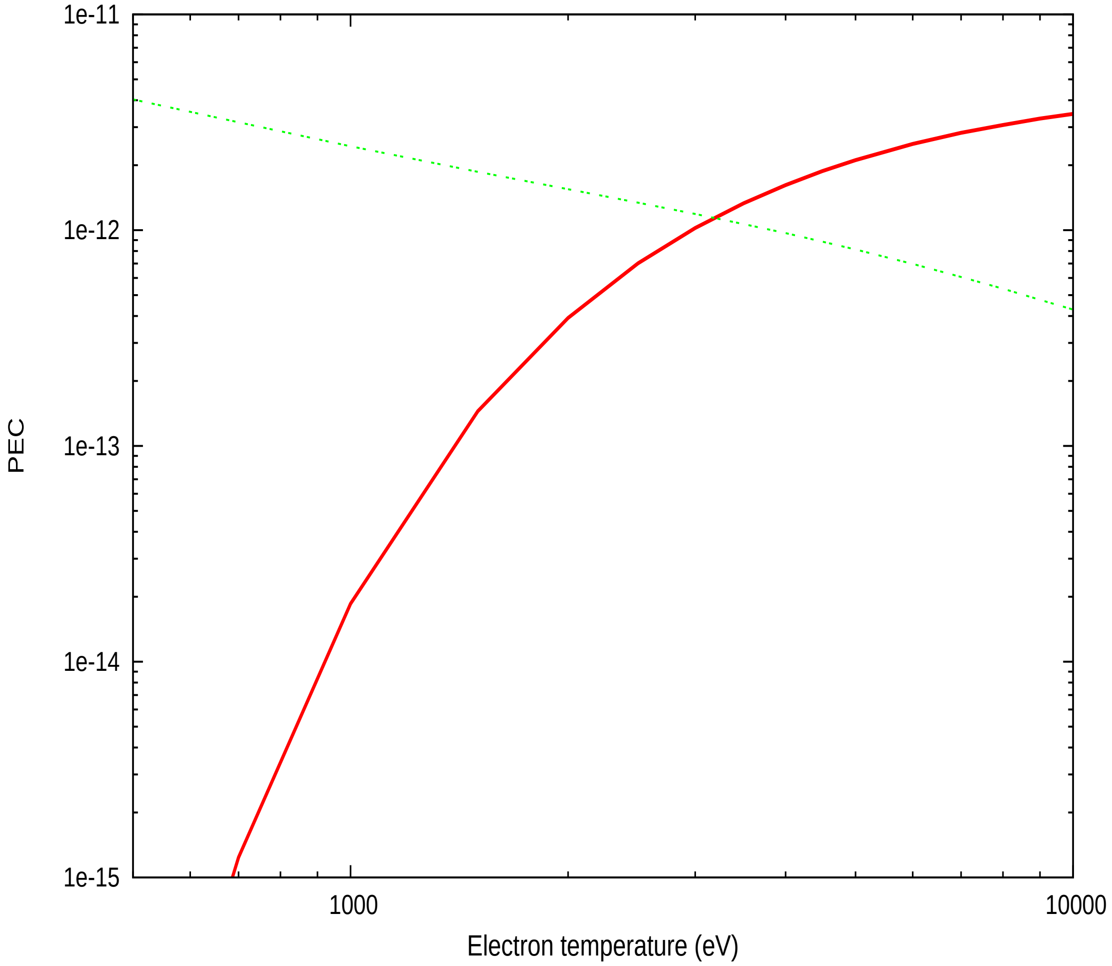

Figure 2.10: PEC^{ex} and PEC^{rec} for Fe Kα. The solid line shows the PEC^{ex} and the dashed line shows the PEC^{rec}.

contributor to the Kα emission in the He-like ion stage. It is clear from the figure that it could easily contribute significantly. We will return to this in chapter 3.

Chapter 3

Spectral Modeling and Abundances

3.1 Fractional Abundances

It is clear from the SNR spectra of W49B that both H-like and He-like Fe are present. The observed intensities from each ion can be used to determine a fractional abundance for these ion stages. However, first one must consider whether the recombination contribution to the line emission of the He-like ion is significant.

Thus, we used our final PEC^{ex} and PEC^{rec} coefficients to analyze the spectra. We use Equation 1.12 to determine the relative abundances of these Fe^{24+} and Fe^{25+}. Note that in this analysis we assume that there is very little bare nuclei of Fe present. We also do not include satellite line contributions to the Kα emission. In our determination of the fractional abundances of Fe we have to assume a temperature for the PEC values. Thus, we show in Table 3.2 the diagnosed abundance of Fe for a range of assumed temperatures. We also show for each temperature what the equilibrium fractional abundance would be. The continuum emission from W49B implies an electron temperature of 1.5-2 keV. Note that the table also shows what abundance would be diagnosed if the recombination contribution to the line emission was omitted.

We used the observed Lyα and Kα intensities for Fe as reported by Hwang et al. [1] and Ozawa et al. [20], these are reproduced in Table 3.1

Considering first the analysis of the emissivities of [1], one can see (comparing columns 2 and 3) that the recombination contribution to the emissivity makes a significant difference at the lowest temperatures. Not including recombination in the spectral modeling would lead one to infer a lower abundance of the H-like ion for a given temperature. The difference is largest at the lowest temperatures, due to the large increase in radiative recombination for

Table 3.1: Table of observed spectral line intensities for W49B, taken from [1] and [20]. Also shown in the table are the range of values of these line intensities, obtained from the fit to the spectrum.

Spectral Line	Intensity from [1] data (10^{-}3 ph cm^{-2} s^{-1})	Intensity from using [20] (10^{-}5 ph cm^{-2} s^{-1})
Fe Lyα	0.024 (0.0013-0.037)	1.46 (1.27-1.65)
Fe Kα	0.83 (0.81-0.86)	5.30 (4.20-6.39)

Table 3.2: Table of diagnosed H-like to He-like ratio for Fe, using the observed Lyα and Kα emission from W49B.

Te(keV)	W49B using [1] data Not including PEC^{rec}	W49B using [1] data Including PEC^{rec}	W49B using [20] Including PEC^{rec}	Equilibrium fraction
1.5	0.065	0.376	0.066	**0.0004**
2.0	0.061	0.081	0.039	**0.0027**
2.5	0.060	0.067	0.035	**0.0088**
3.0	0.058	0.063	0.034	**0.020**
3.5	0.057	0.060	0.033	**0.037**
4.0	0.057	0.059	0.032	**0.061**
4.5	0.056	0.058	0.032	**0.089**

the lowest temperatures. We note that this effect (of omitting the PEC^{rec} in the analysis) would be much more dramatic for elements with lower charge states such as Ar and Ca, which would have significantly more H-like ions present. Using those ions to determine the ionization temperature without accounting for recombination contributions would lead to dramatic overestimations of the temperature.

Comparing next the differences between the fractional abundances using the observations of Ozawa et al. [20], compared with those of Hwang et al. [1] (i.e. comparing columns 3 and 4), one can see that the Ozawa et al. [20] data leads to abundances that are a factor of two lower than those derived from the Hwang et al. [1] data. Note that this is not too surprising, given the large uncertainties in the Lyα flux from the Hwang et al. [1] paper. Thus, this difference is close to being within the expected error bars for this analysis.

In all cases, our evaluated fractional abundances are higher than the collisional ionization equilibrium values, verifying the previous studies that suggested an overionized plasma. In

2005, Kawasaki et al. [23] suggested that photoionization from a hot core plasma could be leading to the overionization of the plasma, with a similar conclusion given by the modeling work of Miceli et al. [2]. However, another possibility is that the free electrons are not Maxwellian, perhaps having a Kappa distribution typical of shock heated plasmas. The presence of a high energy tail in the electron distribution would lead to more H-like ions. It is also possible that the line intensity of the H-like ion stage is being overestimated due to the lack of any satellite lines in the modeling. Both of these issues should be investigated further.

3.2 Elemental Abundances

Given that Fe shows strong signatures from H-like ions, and the results of the previous section showing that the recombination contribution should be included in modeling the He-like Kα feature of Fe, one clearly needs to include recombination in any modeling of He-like Cr and Mn. Thus, we use Equation 1.14 to determine the relative elemental abundances of Cr-to-Fe and Mn-to-Fe for W49B and Cas A. In each case we have to assume a temperature for the theoretical PECs. For each temperature we first evaluate the H-like to He-like fractional abundance for Fe (based upon the Fe Lyα and Kα emission, and assume that Cr and Mn have similar charge state distributions. This results in the elemental abundances shown in Table 3.3 for the observations of Hwang et al. [1], and in Table 3.4 for the observations of Ozawa et al. [20].

Both sets of observations give very similar Cr and Mn abundances. We find that the abundances are consistently larger than the solar ones, in agreement with the previous findings of Hwang et al. [1]. To determine the type of supernova explosion, one can consider the Cr-to-Fe ratio. The Cr-to-Fe ratio favors Type Ia supernova explosion model predictions. However, there are a range of Type Ia models including those that explode at the Chandrasekhar mass [61] and those that explode after a delay, the so-called delayed detonation models [62]. The Chandrasekar mass models predict Cr-to-Fe abundances of less than 1%,

Table 3.3: Table of diagnosed Cr and Mn abundances (relative to Fe) for W49B, using the observations of Hwang et al.[1].

Te(keV)	Cr abundance for W49B using [1] data	Mn abundance for for W49B using [1] data	Solar photospheric abundances Cr / Fe [63]	Solar Photospheric abundances Mn/Fe [63]
1.5	0.0158	0.010	0.01	0.0052
2.0	0.0186	0.011	0.01	0.0052
2.5	0.020	0.012	0.01	0.0052
3.0	0.217	0.012	0.01	0.0052
3.5	0.023	0.012	0.01	0.0052
4.0	0.023	0.013	0.01	0.0052

Table 3.4: Table of diagnosed Cr and Mn abundances (relative to Fe) for W49B, using the observations of Ozawa et al.[20].

Te(keV)	Cr abundance for W49B using [20] data	Mn abundance for for W49B using using[20] data	Solar photospheric abundances Cr / Fe [63]	Solar Photospheric abundances Mn/Fe [63]
1.5	0.0154	0.010	0.01	0.0052
2.0	0.0181	0.011	0.01	0.0052
2.5	0.0201	0.012	0.01	0.0052
3.0	0.214	0.012	0.01	0.0052
3.5	0.022	0.012	0.01	0.0052
4.0	0.023	0.013	0.01	0.0052

while the delayed detonation models predict $> 2\%$. Our results rule out the Chandrasekhar mass explosion models, and are more consistent with the delayed detonation models.

We note that the elemental abundance diagnostics are much less sensitive to the quality of the atomic data. If a PEC is overestimated, as long as the PEC for the other ion in the ratio is also overestimated the diagnosed abundance will not greatly change. For this reason, our diagnosed abundances are similar to those from Hwang et al. [1] despite the large difference in the emissivities used.

Chapter 4

Discussion and Conclusions

Results have been presented of new He-like atomic data for use in spectral modeling of Fe-peak elements. Our final recommended data consist of Dirac *R*-matrix data for the effective collision strengths, calculated A-values and a compilation of previously calculated recombination rate coefficients. It was found that relativistic corrections and radiation damping both can make a significant change to the atomic data. The effects on the predicted Kα features are less sensitive to the atomic data, and we produce a set of photon emissivity coefficients for use in spectral modeling. This data is used to determine the fractional abundance of H-like to He-like Fe in SNR W49B, finding evidence of an overionized plasma. We then determine elemental abundance for Cr and Mn in these plasmas, finding abundances systematically greater than the solar values.

4.1 Future Studies

The method outlined here to determine the elemental abundances would also give the abundances relative to other species. For example, one could determine the abundance of Fe-to-Ar. As in the case described above, this would only work if one had observations from the H-like and He-like ions of these elements. We note that this is commonly done in the literature. However, it is common to either ignore the recombining contribution to the line emission, or to assume equilibrium fractional abundances. The rigorous approach shown here would result in more accurate abundance determinations and provide a better diagnostic of the SN explosion mechanism. We note, however, that for the less charged systems the picture could be complicated by the presence of bare nuclei element and recombining contribution to the H-like emission.

The method outlined here should be used to analyze the spectra for other SNR plasmas that show He-like emission, such as Cas A. Since the fractional abundances depend upon the plasma density and the time since the explosion, this could prove to be a sensitive test of the ionization age of the supernova, particularly if more than one element is used in the analysis.

Before definite conclusions are made on the overionization of these plasmas, other explanations should be explored. These include satellite lines and non-Maxwellian electron distributions. The method outline here to determine elemental abundances should be used for other spectra and should provide the most strict constrains on the explosion mechanism/models. Finally, due to the importance of these diagnostic lines of Cr and Mn, atomic data should be generated for many more of the ion stages. The analysis procedure would be similar to that outlined here, but for different ion stages of the Fe-peak elements. Recent work at Auburn has completed the atomic data for the Ne-like ion stages. This data should be used to study the spectra of Tycho's SNR, Kepler's SNR, and other SNR that show emission from the Ne-like ion stages.

Bibliography

[1] Hwang,U., Petre, R., and Hughes, J.P., The Astrophysical Journal **532**, 970 (2000).

[2] Miceli, M., Decourchelle, A., Ballet, J., Bocchino, F., Hughes, J.P., Hwang, U., Petre, R., Astronomy and Astrophysics **453** 567 (2006)

[3] Yang, X.J., Tsunemi, H., Lu, F..J., Xiao, H.P., and Zhong, J.X., The Astrophysical Journal, **766** 44 (2013)

[4] S.E. Woosley & T.A. Weaver, ARA&A **24** 205 (1986)

[5] S.A. Colgate, The Astrophysical Journal **232** 404 (1979)

[6] A. Saha, A. Sandage, G.A. Tammann, L. Labhardt, F.D. Macchetto, N. Panagia, The Astrophysical Journal **552**, 802 (1999).

[7] W.L. Freedman et al., The Astrophysical Journal **553** 47 (2001)

[8] A.G. Riess et al. The Astrophysical Journal **116** 1009 (1999).

[9] L. Ciotti, A. D'Ercole, S. Pellegrini, and A. Renzini, The Astrophysical Journal **376**, 380 (1991).

[10] A. Ferrara and E. Tolstoy, Mon. Not. R. Astron. Soc **313**, 291 (2000).

[11] S.E. Woosley, T.A. Weaver, The Astrophysical Journal, **423** 371-379(1994)

[12] M. Fink, W. Hillebrandt, F.K. Ropke, Astronomy and Astrophysics **476** 1133 (2007)

[13] Pye, J.P., Thomas, N., Becker, R.H., and Seward, F.D., The Astrophysical Journal, **207** 649 (1994)

[14] Smith, A., Peacock, A., Jones, L.R., and Pye, J.P., The Astrophysical Journal, **296** 469 (1985s)

[15] Fujimoto, R., et al., Publ. Astron. Soc. Japan, **47**, L31 (1995)

[16] Radhakrishnan, V., Goss, W.M., Murray, J.D., and Brooks, J.W., The Astrophysical Journal Supplement Series, **24**, 49 (1972)

[17] Tamagawa, T., et al., Publications of the Astronomical Society of Japan **61** S167 (2009)

[18] Yang, X.J., Tsunemi, H., Lu, F..J., Chen, L., The Astrophysical Journal, **692** 894 (2009)

[19] Park, S. et al. The Astrophysical Journal **767**, L10 (2013)

[20] Ozawa, M., Koyama, K., Yamaguchi, H., Masai, K., Tamagawa, T. The Astrophysical Journal **706**, L71 (2009)

[21] Raymond, J.C. & Smith, B.W., The Astrophysical Journal Supplement **35** 419 (1977).

[22] Gu, M.F., Astrophysical Journal **582** 1241 (2003)

[23] Kawasaki, M., Ozaki, M., Nagase, F., Inoue, H., and Petre, R., The Astrophysical Journal, **631**, 935 (2005)

[24] Malespin, C., Ballance, C.P., Pindzola, M.S., Witthoeft, M.C., Kallman, T.R., and Loch, S.D., Astronomy and Astrophysics, **526** A115 (2011)

[25] Summers, H.P., Dickson, W.J., O'Mullane, M.G., Badnell, N.R., Whiteford, A.D., Brooks, D.H., Lang, J., Loch, S.D., Griffin D.C., Plasma Physics and Controlled Fusion **48** 263 (2006)

[26] Thorn, D.B., Beiersdorfer, P., Brown, G.V., Kelley, R.L., Kilbourne, C.A., and Porter, F.S., Journal of Physics: Conference Series **163** 012036 (2009)

[27] Wong, K.K., Beiersdorfer, P., Reed, K.J., Vogel, D.A., Phys. Rev. A **51** 1214 (1995)

[28] Sampson, D.H., Goett, S.J. and Clark, R.E.H., At. Data Nucl. Data Tables **29** 467 (1983)

[29] Zhang, H.L. and Sampson, D.H., The Astrophysical Journal Supplement Series **63** 487 (1987)

[30] Zhang, H.L., Sampson, D.H., and Clark, R.E.H., Phys. Rev. A **41** 198 (1990)

[31] Pradhan, A.K., Phys. Rev. A **28** 2113 (1983a)

[32] Pradhan, A.K., Phys. Rev. A **28** 2128 (1983b)

[33] Pradhan, A.K., The Astrophysical Journal Supplement Series **59** 183 (1985)

[34] Keenan, F.P., S.M. McCann, and Kingston, A.E., Physica Scripta **35** 432 (1987)

[35] Zhang, H.L. and Pradhan, A.K., J. Phys. B, **28** L285 (1995)

[36] Kimura, E., Nakazaki, S., Berrington, K.A., and Norrington, P.H., J. Phys. B **33** 3449 (2000)

[37] Whiteford, A.D., Badnell, N.R., Ballance, C.P., O'Mullane, M.G., Summers, H.P., and Thomas, A.L., J. Phys. B **34** 3179 (2001)

[38] Griffin, D.C., Badnell, N.R., and Pindzola, M.S., J. Phys. B **31** 3713 (1998)

[39] Griffin, D.C. and Ballance, C.P., J. Phys. B **42** 235201 (2009)

[40] Aggarwal, K.M. and Keenan, F.P., Phys. Scr. **85** 065301 (2012)

[41] Aggarwal, K.M. and Keenan, F.P., Phys. Scr. **87** 055302 (2012) 3

[42] C. Badenes, E. Bravo, and J.P. Hughes, The Astrophysical Journal **680**, L33 (2008).

[43] J.Oelgoetz, C.J. Fontes, C. J., H.L. Zhang, M. Montenegro, S.N. Nahar, A.K. Pradhan, Mon. Not. R. Astron. Soc **382** 761 (2007)

[44] Bates, D.R., Kingston, A.E., & McWhirter, R.W.P. Proc. Royal Soc. London. **267** 297 (1962)

[45] Griffin, D.C., Badnell, N.R., & Pindzola, M.S., J. Phys. B. **31** 3713 (1998)

[46] Dyall, K.G., Grant, I.P., Johnson, C.T., Parpia, F.A., and Plummer, E.P., Comput. Phys. Commun. **55** 425 (1989)

[47] Parpia, F. A., Froese Fischer, C., & Grant, I. P., Comput. Phys. Commun., **94** 249 (1996)

[48] Robicheaux, R., Gorczyca, T.W, Pindzola, M.S., Badnell, N.R., Phys. Rev A **52** 1319 (1995).

[49] Wigner, E.P., Physics Review, **70** 606 (1946).

[50] Wigner, E.P. and Eisenbud, L., Physics Review **72** 29 (1947).

[51] Badnell, N.R., J. Phys. B **19** 3827 (1986)

[52] Mitnik, D.M., Griffin, D.C., Ballance, C.P., & Badnell, N.R. J. Phys. B. **36**, 717 (2003)

[53] Ballance, C.P. & Griffin, D.C., J. Phys. B. **37** 2943 (2004)

[54] Berrington, K.A., Eissner, W.B., & Norrington, P.H., Comput. Phys. Commun. **92** 290 (1995)

[55] Burgess, A., J. Phys. B **7** L364 (1970)

[56] Ralchenko, Yu., Kramida, A.E., Reader, J., and NIST ASD Team (2008). NIST Atomic Spectra Database (version 3.1.5), [Online]. Available: http://physics.nist.gov/asd3 [2010, April 4]. National Institute of Standards and Technology, Gaithersburg, MD.

[57] Ballance, C.P. and Griffin, D.C., J. Phys. B **39** 3617 (2006)

[58] Norrington, P.H. and Grant, I.P., J. Phys. B **20** 4869 (1987)

[59] Smith, R.K., Brickhouse, N.S., Liedahl, D.A., and Raymond, J.C., The Astrophysical Journal, **556**, L91 (2001)

[60] Derevianko, A., Johnson, W. R., Physical Review A **56(2)** 1288 (1997)

[61] Nomoto, K., et al., Nuclear Physics A, **621**, 467 (1997)

[62] Travaglio, C., Hillebrandt, C., Reinecke, M., and Thielemann, F.K., Astronomy and Astrophysics, **425**, 1029 (2004)

[63] Anders, L. and Grevesse, N., Geochim. Cosmochim. Acta, **53**, 197 (1989)

Appendices

Appendix A - Tables of the energies and A-values

Table 1: Level energies from NIST compared to Aggarwal (2012) [40] and present energies for Fe^{24+}. Energies are in units of Rydbergs. Differences shown are percent differences between our results and those from NIST. Also included, is a comparison of our ICFT energy data to our DARC energy data.

Configuration	Term	Level	NIST	Aggarwal	Present Work	ICFT	Difference (%)	Difference (% ICFT-DARC)
$1s^2$	^1S	0	0.00000	0.00000	0.00000	0.00000	0.0000	N/A
$1s2s$	^3S	1	487.78084	488.25922	488.27305	488.50962	0.1009	0.0485
$1s2p$	^3P	0	489.90883	490.27246	490.28515	490.46228	0.0768	0.0361
$1s2p$	^3P	1	490.09063	490.52689	490.53876	490.74388	0.0914	0.0418
$1s2s$	^1S	0	490.05728	490.54865	490.56142	490.78311	0.1029	0.0452
$1s2p$	^3P	2	491.14200	491.65524	491.66751	491.86216	0.1070	0.0396
$1s2p$	^1P	1	492.47140	493.00031	493.01425	493.25347	0.1102	0.0485
$1s3s$	^3S	1	577.94110	578.44208	578.45578	578.71219	0.0891	0.0443
$1s3p$	^3P	0	578.52790	578.99860	579.01206	579.24556	0.0837	0.0403
$1s3s$	^1S	0	578.55400	579.04279	579.05590	579.28357	0.0868	0.0393
$1s3p$	^3P	1	578.56980	579.07642	579.08990	579.32102	0.0899	0.0399
$1s3p$	^3P	2	578.89420	579.40662	579.41990	579.64472	0.0908	0.0388
$1s3d$	^3D	2	579.21320	579.71643	579.73008	579.96152	0.0892	0.0399
$1s3d$	^3D	1	579.20770	579.72394	579.73759	579.95345	0.0915	0.0372
$1s3p$	^1P	1	579.25420	579.76978	579.78342	580.00817	0.0914	0.0388
$1s3d$	^3D	3	579.33070	579.84576	579.85941	580.08765	0.0913	0.0394
$1s3d$	^1D	2	579.35170	579.85907	579.87274	580.10206	0.0899	0.0395
$1s4s$	^3S	1	609.15380	609.66852	609.68221	609.93258	0.0867	0.0411
$1s4p$	^3P	0	609.39980	609.89758	609.91118	610.15088	0.0839	0.0393
$1s4s$	^1S	0	609.41000	609.91315	609.92660	610.15377	0.0848	0.0372
$1s4p$	^3P	1	609.41800	609.92987	609.94345	610.18026	0.0862	0.0388
$1s4p$	^3P	2	609.55470	610.06927	610.08280	610.31159	0.0866	0.0375
$1s4d$	^3D	2	609.68960	610.19635	610.20995	610.43600	0.0853	0.0370
$1s4d$	^3D	1	609.68690	610.20026	610.21389	610.44003	0.0864	0.0371
$1s4p$	^1P	1	609.70690	610.21808	610.23171	610.45616	0.0861	0.0368
$1s4d$	^3D	3	609.73880	610.25092	610.26457	609.49756	0.0862	0.1257
$1s4f$	^1D	2	609.74790	610.25824	610.27188	610.49187	0.0859	0.0360
$1s4f$	^3F	2		610.25854	610.27220	610.49820	N/A	0.0370
$1s4d$	^3F	3		610.25861	610.27227	610.49879	N/A	0.0371
$1s4f$	^3F	4		610.28571	610.29936	610.52643	N/A	0.0372
$1s4f$	^1F	3		610.28577	610.29945	610.52701	N/A	0.0373
$1s5s$	^3S	1	623.52350	624.03802	624.05170		0.0847	
$1s5p$	^3P	0	623.64629	624.15387	624.16749		0.0836	
$1s5s$	^1S	0	623.65390	624.16187	624.17544		0.0836	
$1s5p$	^3P	1	623.65840	624.17029	624.18391		0.0843	
$1s5p$	^3P	2	623.72860	624.24164	624.25520		0.0844	
$1s5d$	^3D	1		624.30579	624.31940		N/A	
$1s5d$	^3D	2		624.30792	624.32158		N/A	
$1s5p$	^1P	1	623.80600	624.31708	624.33075		0.0841	
$1s5d$	^3D	3		624.33374	624.34737		N/A	
$1s5d$	^1D	2		624.33783	624.35149		N/A	
$1s5f$	^3F	2		624.33801	624.35164		N/A	
$1s5f$	^3F	3		624.33801	624.35169		N/A	
$1s5f$	^3F	4		624.35187	624.36555		N/A	
$1s5f$	^1F	3		624.35199	624.36563		N/A	
$1s5g$	^3G	3		624.35199	624.36564		N/A	
$1s5g$	^3G	4		624.35199	624.36564		N/A	
$1s5g$	^3G	5		624.36029	624.37397		N/A	
$1s5g$	^1G	4		624.36029	624.37397		N/A	

Table 2: Level energies from NIST compared to Aggarwal (2012) [40] and present energies for Co^{25+}. Energies are in units of Rydbergs. Differences shown are percent differences between our results and those from NIST. Also included, is a comparison of our ICFT energy data to our DARC energy data.

Configuration	Term	Level	NIST	Aggarwal	Present Work	ICFT	Difference (%)	Difference (% ICFT-DARC)
$1s^2$	^1S	0	0.00000	0.00000	0.00000	0.00000	0.0000	N/A
$1s2s$	^3S	1	527.23524	527.79962	527.81423	528.05451	0.1098	0.0455
$1s2p$	^3P	0	529.46520	529.90009	529.91360	530.08723	0.0847	0.0328
$1s2p$	^3P	1	529.65300	530.16492	530.17756	530.39935	0.0990	0.0418
$1s2s$	^1S	0	529.62549	530.20630	530.21995	530.43066	0.1122	0.0397
$1s2p$	^3P	2	530.91494	531.51825	531.53128	531.72214	0.1161	0.0359
$1s2p$	^1P	1	532.28412	532.90063	532.91539	533.15274	0.1186	0.0445
$1s3s$	^3S	1	624.76000	625.35107	625.36553	625.62483	0.0969	0.0415
$1s3p$	^3P	0	625.37980	625.93170	625.94603	626.18045	0.0905	0.0375
$1s3s$	^1S	0	625.40800	625.97729	625.99122	626.22045	0.0933	0.0366
$1s3p$	^3P	1	625.42540	626.01770	626.03203	626.26357	0.0970	0.0370
$1s3p$	^3P	2	625.81080	626.40930	626.42341	626.64544	0.0979	0.0354
$1s3d$	^3D	2	626.14340	626.73218	626.74662	626.97481	0.0963	0.0364
$1s3d$	^3D	1	626.13710	626.74011	626.75454	626.96606	0.0986	0.0337
$1s3p$	^1P	1	626.18170	626.78253	626.79696	627.01856	0.0983	0.0354
$1s3d$	^3D	3	626.28190	626.88354	626.89798	627.12293	0.0984	0.0359
$1s3d$	^1D	2	626.30380	626.89734	626.91181	627.13794	0.0971	0.0361
$1s4s$	^3S	1	658.53600	659.13477	659.14921	659.40112	0.0931	0.0382
$1s4p$	^3P	1	658.79410	659.37372	659.38814	659.62800	0.0902	0.0364
$1s4s$	^1S	0	658.80510	659.38965	659.40392	659.63112	0.0909	0.0345
$1s4p$	^3P	1	658.81420	659.40930	659.42375	659.66049	0.0925	0.0359
$1s4p$	^3P	2	658.97640	659.57471	659.58902	659.81487	0.0930	0.0342
$1s4d$	^3D	2	659.11670	659.70709	659.72153	659.94424	0.0918	0.0338
$1s4d$	^3D	1	659.11400	659.71124	659.72570	659.94862	0.0928	0.0338
$1s4p$	^1P	1	659.13310	659.72754	659.74202	659.96362	0.0924	0.0336
$1s4d$	^3D	3	659.17500	659.77100	659.78545	660.00924	0.0926	0.0339
$1s4f$	^3F	2	659.18420	659.77856	659.79302	660.01736	0.0924	0.0340
$1s4f$	^3F	2		659.77893	659.79342	660.01612	N/A	0.0338
$1s4d$	^3F	3		659.77899	659.79349	660.01674	N/A	0.0338
$1s4f$	^3F	4		659.81073	659.82519	660.04924	N/A	0.0340
$1s4f$	^1F	3		659.81079	659.82529	660.04924	N/A	0.0339
$1s5s$	^3S	1	674.08200	674.68115	674.69565		0.0910	
$1s5p$	^3P	0	674.20430	674.80206	674.81648		0.0908	
$1s5s$	^1S	0	674.21900	674.81018	674.82456		0.0898	
$1s5p$	^3P	1	674.22370	674.82013	674.83457		0.0906	
$1s5p$	^3P	2	674.30660	674.90472	674.91914		0.0908	
$1s5d$	^3D	1		674.97162	674.98605		N/A	
$1s5d$	^3D	2		674.97388	674.98835		N/A	
$1s5p$	^1P	1	674.38680	674.98230	674.99674		0.0904	
$1s5d$	^3D	3		675.00433	675.01878		N/A	
$1s5d$	^1D	2		675.00861	675.02304		N/A	
$1s5f$	^3F	2		675.00879	675.02324		N/A	
$1s5f$	^3F	3		675.00885	675.02329		N/A	
$1s5f$	^3F	4		675.02502	675.03952		N/A	
$1s5f$	^1F	3		675.02515	675.03959		N/A	
$1s5g$	^3G	3		675.02515	675.03960		N/A	
$1s5g$	^3G	4		675.02515	675.03960		N/A	
$1s5g$	^3G	5		675.03491	675.04935		N/A	
$1s5g$	^1G	4		675.03491	675.04935		N/A	

Table 3: Level energies from NIST compared to Aggarwal (2012) [40] and present energies for Ni^{26+}. Energies are in units of Rydbergs. Differences shown are percent differences between our results and those from NIST. Also included, is a comparison of our ICFT energy data to our DARC energy data.

Configuration	Term	Level	NIST	Aggarwal	Present Work	ICFT	Difference (%)	Difference (% ICFT-DARC)
$1s^2$	^1S	0	0.00000	0.00000	0.00000	0.00000	0.0000	N/A
$1s2s$	^3S	1	568.26313	568.92120	568.93659	569.18002	0.1185	0.0428
$1s2p$	^3P	0	570.59706	571.10980	571.12420	571.29329	0.0924	0.0296
$1s2p$	^3P	1	570.79062	571.38495	571.39835	571.63663	0.1065	0.0417
$1s2s$	^1S	0	570.76811	571.44672	571.46127	571.66150	0.1214	0.0350
$1s2p$	^3P	2	572.29111	572.99255	573.00641	573.19174	0.1250	0.0323
$1s2p$	^1P	1	573.69993	574.41168	574.42717	574.66107	0.1268	0.0407
$1s3s$	^3S	1	673.45400	674.14294	674.15822	674.42018	0.1046	0.0389
$1s3p$	^3P	0	674.09700	674.74805	674.76317	674.99694	0.0988	0.0346
$1s3s$	^1S	0	674.12620	674.79492	674.80966	675.04033	0.1014	0.0342
$1s3p$	^3P	1	674.14530	674.84235	674.85747	675.08779	0.1056	0.0341
$1s3p$	^3P	2	674.60010	675.30383	675.31876	675.53624	0.1065	0.0322
$1s3d$	^3D	2	674.94730	675.63977	675.65500	675.87849	0.1049	0.0331
$1s3d$	^3D	1	674.93900	675.64807	675.66332	675.86929	0.1073	0.0305
$1s3p$	^1P	1	674.98190	675.68695	675.70220	675.91925	0.1067	0.0321
$1s3d$	^3D	3	675.10850	675.81586	675.83110	676.05121	0.1070	0.0326
$1s3d$	^1D	2	675.13220	675.83014	675.84543	676.06675	0.1056	0.0327
$1s4s$	^3S	1	709.88340	710.58813	710.60344	710.85582	0.1014	0.0355
$1s4p$	^3P	0	710.15220	710.83722	710.85242	711.09106	0.0986	0.0336
$1s4s$	^1S	0	710.16320	710.85345	710.86854	711.09444	0.0993	0.0318
$1s4p$	^3P	1	710.17320	710.87616	710.89141	711.12689	0.1011	0.0331
$1s4p$	^3P	2	710.36460	711.07104	711.08621	711.30806	0.1016	0.0312
$1s4d$	^3D	2	710.51130	711.20880	711.22408	711.44190	0.1003	0.0306
$1s4d$	^3D	1	710.50760	711.21320	711.22847	711.44663	0.1015	0.0307
$1s4p$	^1P	1	710.52590	711.22797	711.24324	711.46015	0.1010	0.0305
$1s4d$	^3D	3	710.57960	711.28320	711.29845	711.51761	0.1012	0.0308
$1s4f$	^1D	2	710.58960	711.29102	711.30629	711.52640	0.1009	0.0309
$1s4f$	^3F	2		711.29150	711.30675	711.52437	N/A	0.0306
$1s4d$	^3F	3		711.29156	711.30682	711.52504	N/A	0.0307
$1s4f$	^3F	4		711.32843	711.34372	711.56291	N/A	0.0308
$1s4f$	^1F	3		711.32855	711.34382	711.56291	N/A	0.0308
$1s5s$	^3S	1	726.65300	727.35931	727.37458		0.0993	
$1s5p$	^3P	0	726.78930	727.48523	727.50048		0.0979	
$1s5s$	^1S	0	726.79650	727.49353	727.50869		0.0980	
$1s5p$	^3P	1	726.80200	727.50500	727.52029		0.0988	
$1s5p$	^3P	2	726.90040	727.60474	727.61996		0.0990	
$1s5d$	^3D	1		727.67432	727.68957		N/A	
$1s5d$	^3D	2		727.67676	727.69200		N/A	
$1s5p$	^1P	1	726.98240	727.68433	727.69958		0.0987	
$1s5d$	^3D	3		727.71240	727.72766		N/A	
$1s5d$	^1D	2		727.71680	727.73207		N/A	
$1s5f$	^3F	2		727.71704	727.73230		N/A	
$1s5f$	^3F	3		727.71710	727.73236		N/A	
$1s5f$	^3F	4		727.73596	727.75124		N/A	
$1s5f$	^1F	3		727.73602	727.75132		N/A	
$1s5g$	^3G	3		727.73608	727.75133		N/A	
$1s5g$	^3G	4		727.73608	727.75133		N/A	
$1s5g$	^3G	5		727.74738	727.76267		N/A	
$1s5g$	^1G	4		727.74738	727.76267		N/A	

Table 4: Table of radiative rates (A_{ji} in s^{-1}) for Fe XXV transitions from the ground to the n=2 shell.

Transition	Present Work	Aggarwal (2012)	NIST
$1s2s(^3S_1) \rightarrow 1s^2\ (^1S_0)$	2.0200×10^{8}	2.0200×10^{8}	2.1200×10^{8}
$1s2p(^3P_1) \rightarrow 1s^2\ (^1S_0)$	3.9300×10^{13}	4.438×10^{13}	4.4200×10^{13}
$1s2p(^3P_2) \rightarrow 1s^2\ (^1S_0)$	6.5300×10^{9}	6.492×10^{9}	6.6400×10^{9}
$1s2p(^1P_1) \rightarrow 1s^2\ (^1S_0)$	4.7200×10^{14}	4.656×10^{14}	4.5700×10^{14}

Table 5: Table of radiative rates (A_{ji} in s^{-1}) for Co XXVI transitions from the ground to the n=2 shell.

Transition	Present Work	Aggarwal (2012)	NIST
$1s2s(^3S_1) \rightarrow 1s^2\ (^1S_0)$	2.9800×10^{8}	2.9750×10^{8}	3.1200×10^{8}
$1s2p(^3P_1) \rightarrow 1s^2\ (^1S_0)$	5.2700×10^{13}	5.919×10^{13}	5.8900×10^{13}
$1s2p(^3P_2) \rightarrow 1s^2\ (^1S_0)$	8.9000×10^{9}	8.850×10^{9}	9.0500×10^{9}
$1s2p(^1P_1) \rightarrow 1s^2\ (^1S_0)$	5.4400×10^{14}	5.361×10^{14}	5.2600×10^{14}

Table 6: Table of radiative rates (A_{ji} in s^{-1}) for Ni XXVII transitions from the ground to the n=2 shell.

Transition	Present Work	Aggarwal (2012)	NIST
$1s2s(^3S_1) \rightarrow 1s^2\ (^1S_0)$	4.3300×10^{8}	4.3220×10^{8}	4.5200×10^{8}
$1s2p(^3P_1) \rightarrow 1s^2\ (^1S_0)$	6.9300×10^{13}	7.743×10^{13}	7.7000×10^{13}
$1s2p(^3P_2) \rightarrow 1s^2\ (^1S_0)$	1.2000×10^{10}	1.193×10^{10}	1.2200×10^{9}
$1s2p(^1P_1) \rightarrow 1s^2\ (^1S_0)$	6.2300×10^{14}	6.135×10^{14}	6.0200×10^{14}

Appendix B - Collision strength figures

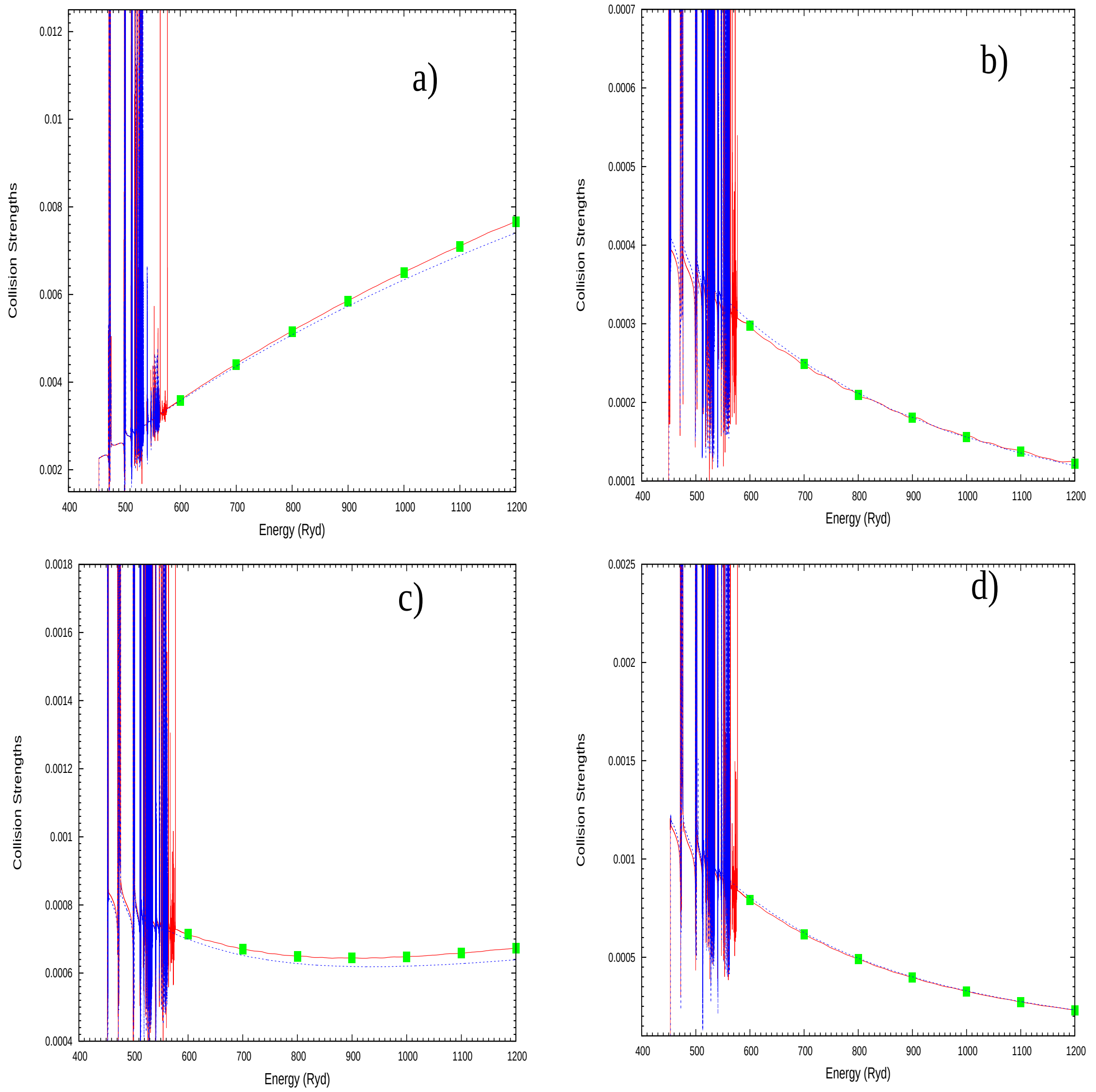

Figure 1: Collision strength for the a)1s^2 ($^1S_0$) $\rightarrow$ 1s2p($^1P_1$) b)1s^2 ($^1S_0$) $\rightarrow$ 1s2s($^3S_1$) c)1s^2 ($^1S_0$) $\rightarrow$ 1s2p($^3P_1$) d)1s^2 ($^1S_0$) $\rightarrow$ 1s2p($^3P_2$) transitions for Mn^{23+}. The solid line (red) shows the DARC damped calculation, the dashed line (blue) shows the ICFT damped calculation, and the results of Aggarwal and Keenan [40] are shown by solid squares.

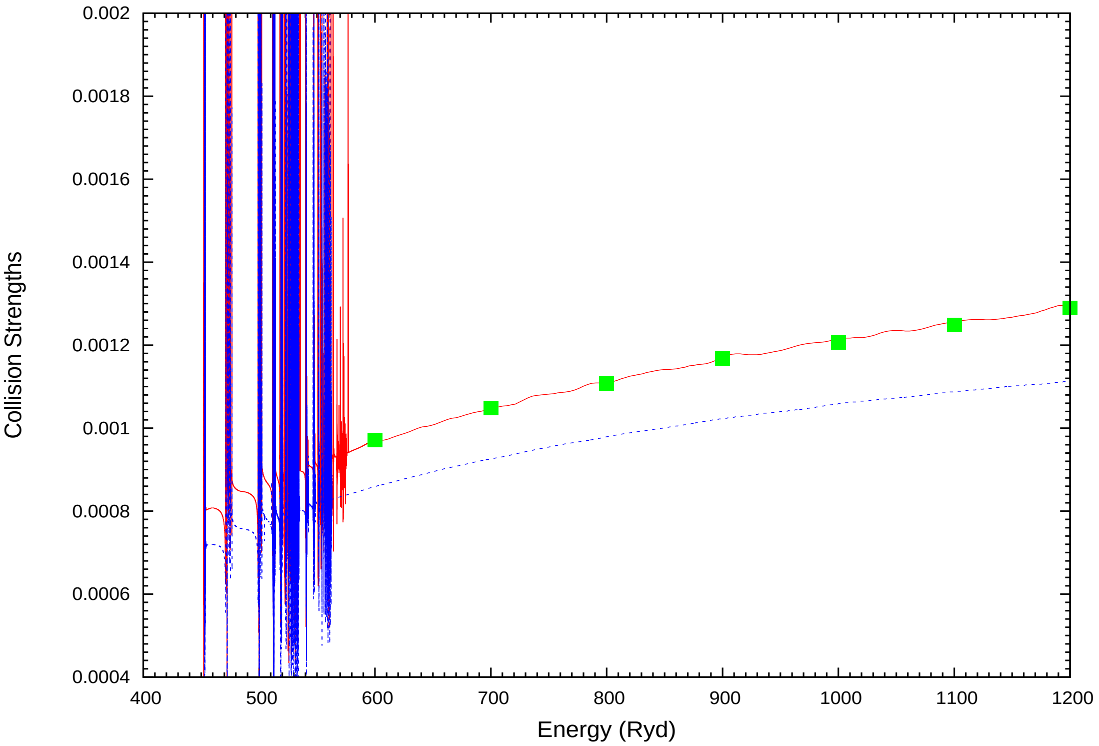

Figure 2: Effective collision strength for the $1s^2$ ($^1S_0$) → $1s2s(^1S_0)$ transition for Mn^{23+}. The solid line (red) shows the DARC damped calculation and the dashed line shows the DARC undamped calculations. The ICFT damped calculations are shown by the dotted line (blue). The results of Aggarwal and Keenan [40] are shown by squares.

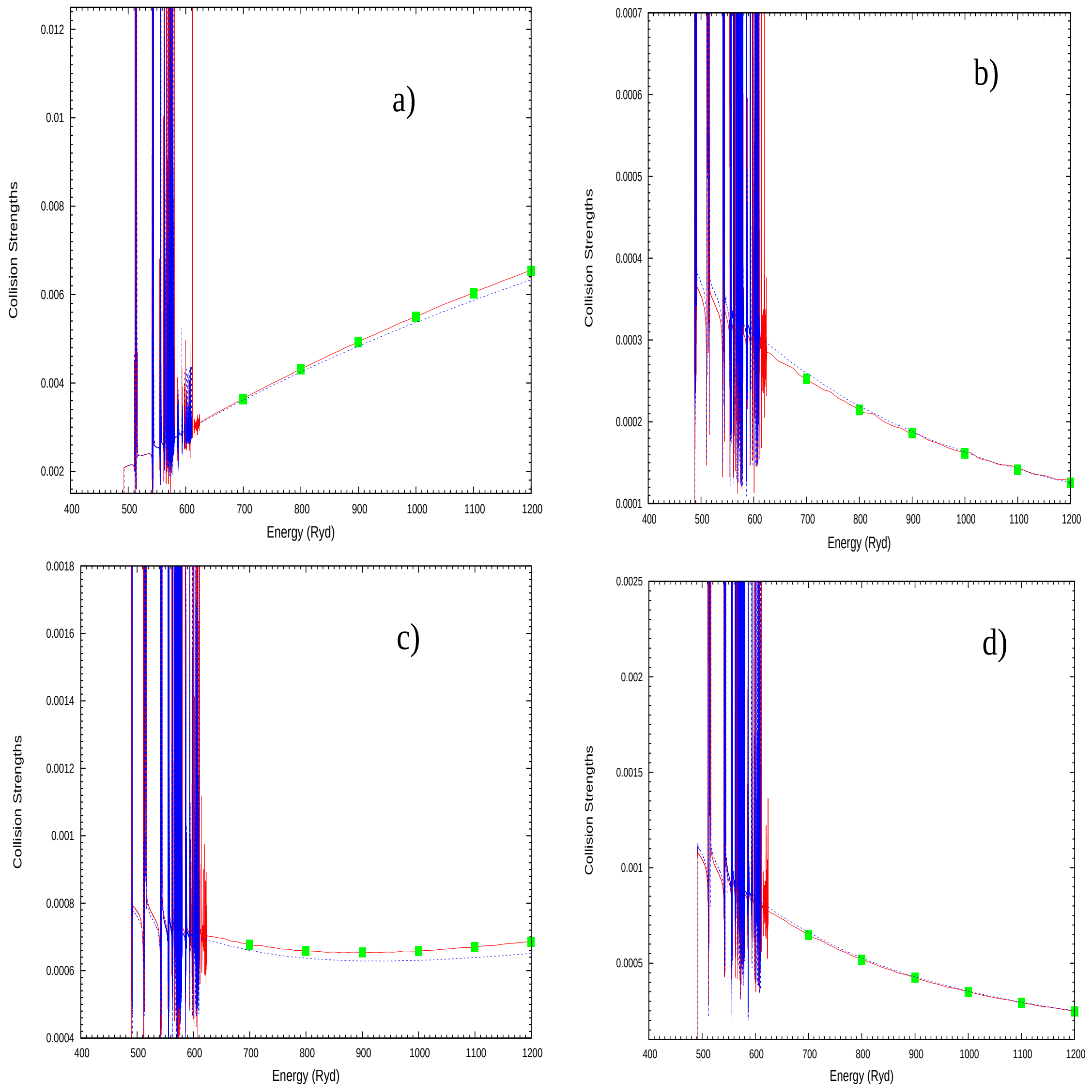

Figure 3: Collision strength for the a)$1s^2$ ($^1S_0$) → $1s2p(^1P_1)$ b)$1s^2$ ($^1S_0$) → $1s2s(^3S_1)$ c)$1s^2$ ($^1S_0$) → $1s2p(^3P_1)$ d)$1s^2$ ($^1S_0$) → $1s2p(^3P_2)$ transitions for Fe^{24+}. The solid line (red) shows the DARC damped calculation, the dashed line (blue) shows the ICFT damped calculation, and the results of Aggarwal and Keenan [40] are shown by solid squares.

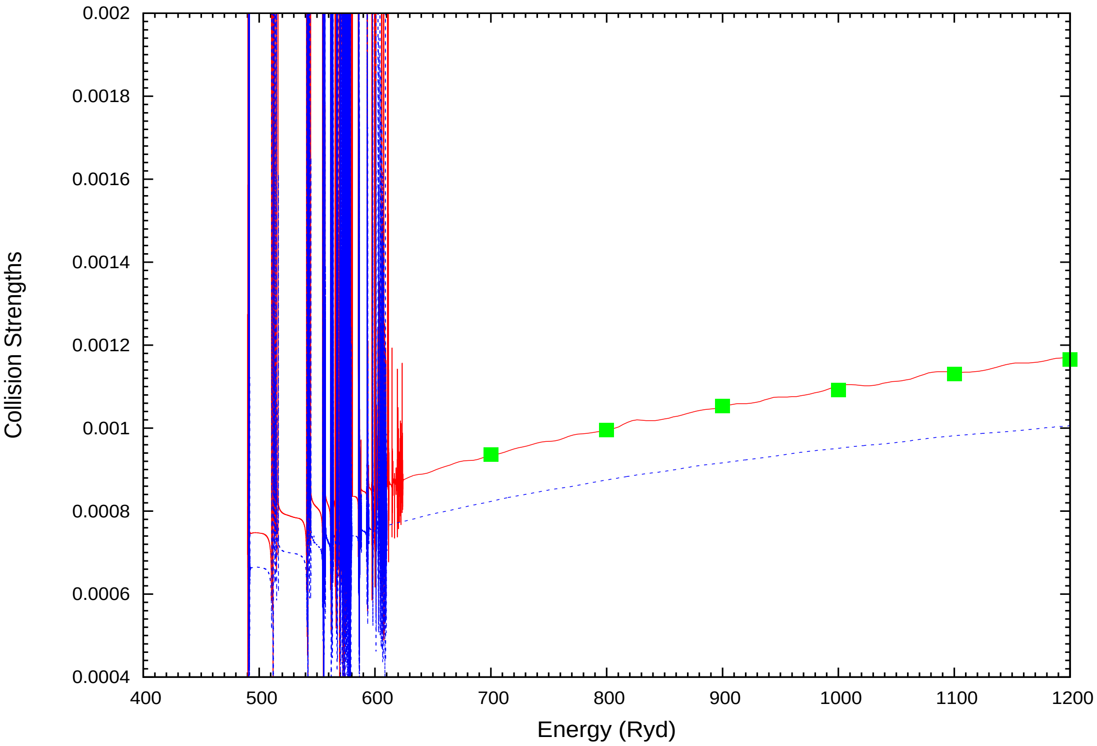

Figure 4: Effective collision strength for the $1s^2$ ($^1S_0$) → $1s2s(^1S_0)$ transition for Fe^{24+}. The solid line (red) shows the DARC damped calculation and the dashed line shows the DARC undamped calculations. The ICFT damped calculations are shown by the dotted line (blue). The results of Aggarwal and Keenan [40] are shown by squares.

Appendix C - Effective collision strength figures

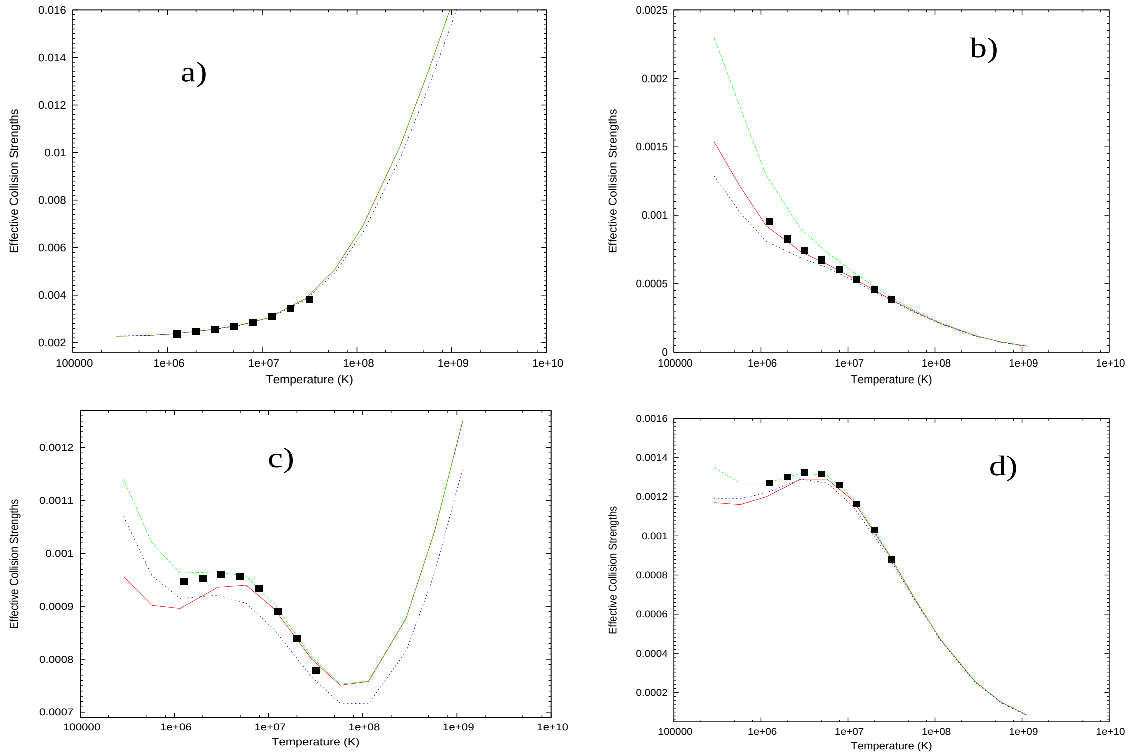

Figure 5: Effective collision strength for the a) $1s^2(^1S_0) \rightarrow 1s2p(^1P_1)$ b) $1s^2(^1S_0) \rightarrow 1s2s(^3S_1)$ c) $1s^2(^1S_0) \rightarrow 1s2p(^3P_1)$ d) $1s^2(^1S_0) \rightarrow 1s2p(^3P_2)$ transitions for Mn^{23+}. The solid line (red) shows the DARC damped calculation, the green line shows the DARC undamped calculation and the blue line shows the ICFT damped calculation. The results of Aggarwal and Keenan [40] are shown by solid squares. Note that in figure a) the calculations all give very similar results and cannot be resolved on the plot.

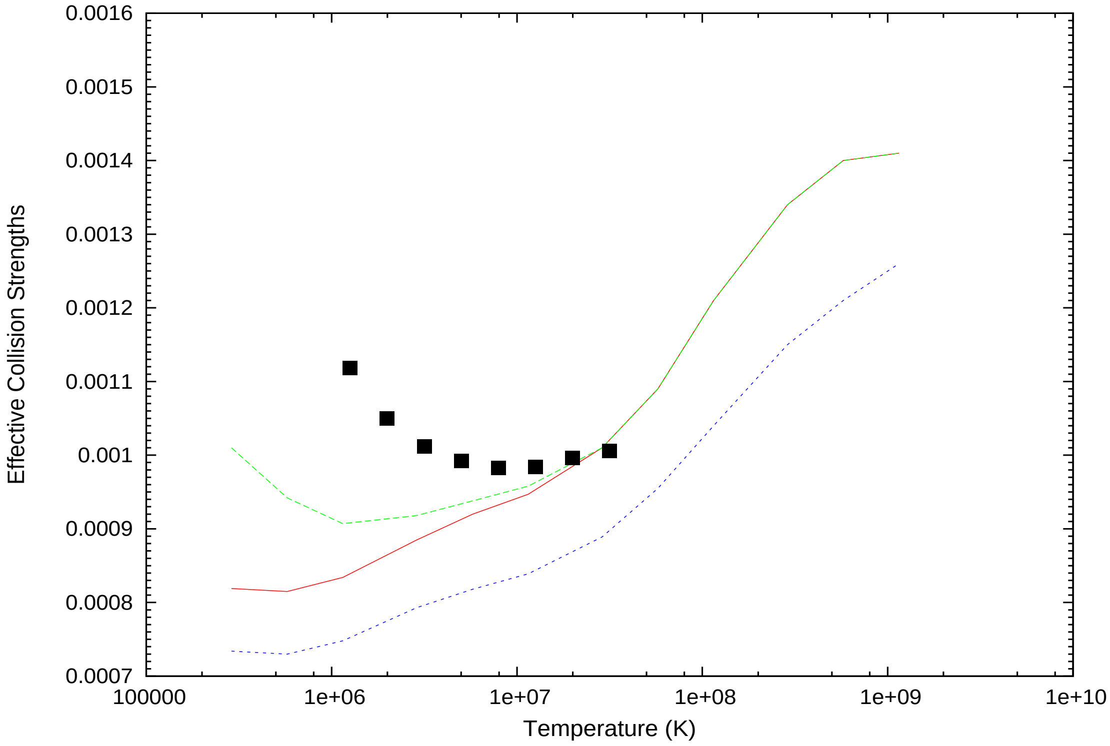

Figure 6: Effective collision strength for the $1s^2$ ($^1S_0$) → $1s2s(^1S_0)$ transition for Mn^{23+}. The solid red line shows the DARC damped calculation and the green line shows the DARC undamped calculations. The ICFT damped calculations are shown by the blue line. The results of Aggarwal and Keenan [40] are shown by squares.

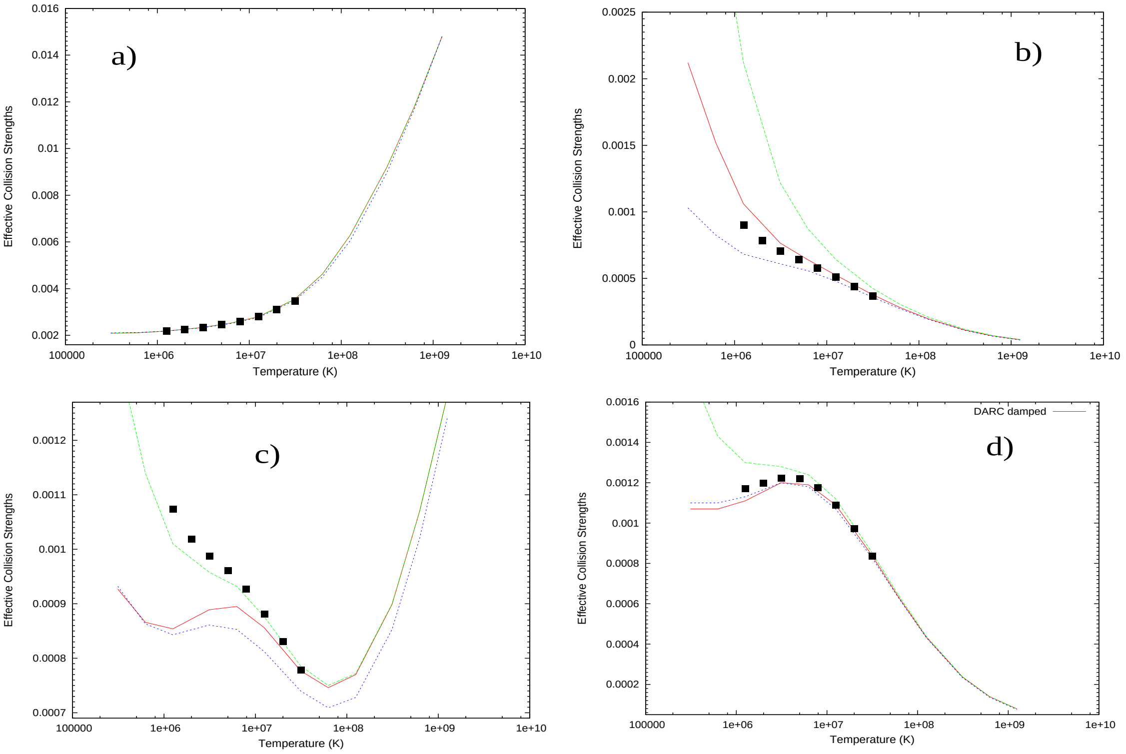

Figure 7: Effective collision strength for the a) $1s^2(^1S_0) \rightarrow 1s2p(^1P_1)$ b) $1s^2(^1S_0) \rightarrow 1s2s(^3S_1)$ c) $1s^2(^1S_0) \rightarrow 1s2p(^3P_1)$ d) $1s^2(^1S_0) \rightarrow 1s2p(^3P_2)$ transitions for Fe^{24+}. The solid line shows the DARC damped calculation (red), the green line shows the DARC undamped calculation and the blue line shows the ICFT damped calculation. The results of Aggarwal and Keenan [40] are shown by solid squares. Note that in figure a) the calculations all give very similar results and cannot be resolved on the plot.

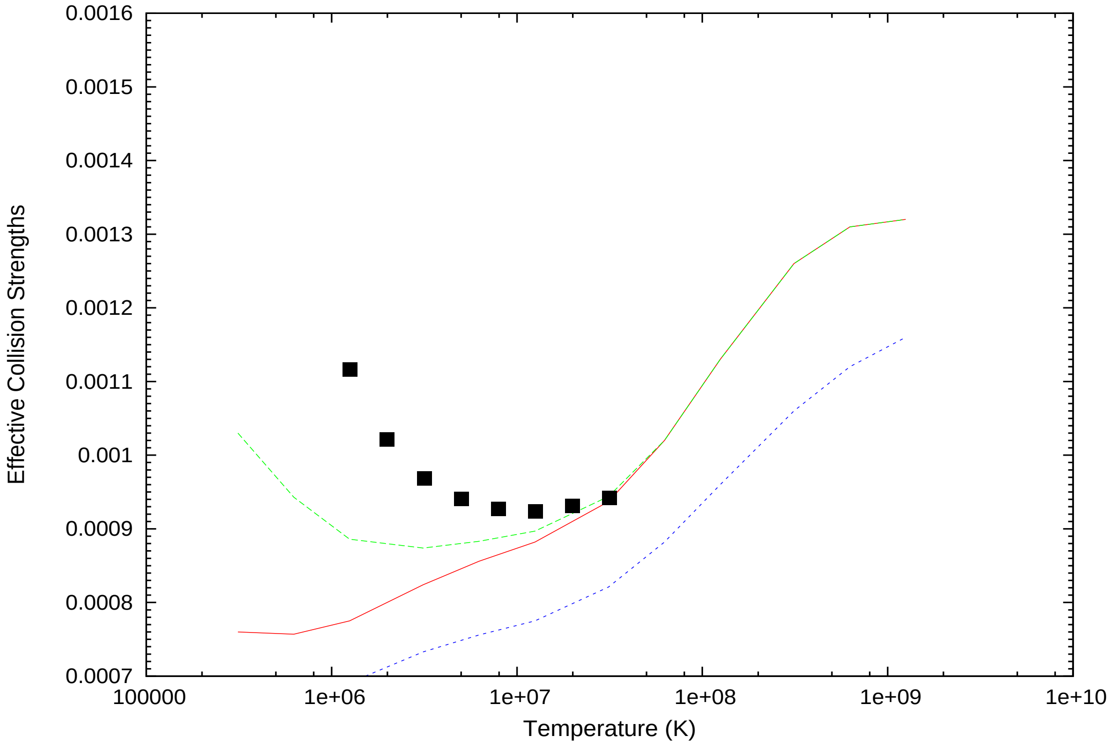

Figure 8: Effective collision strength for the $1s^2$ $(^1S_0) \rightarrow 1s2s(^1S_0)$ transition for Fe^{24+}. The solid red line shows the DARC damped calculation and the green line shows the DARC undamped calculations. The ICFT damped calculations are shown by the blue line. The results of Aggarwal and Keenan [40] are shown by squares.